

An adaptive viscosity regularization approach for the numerical solution of conservation laws: Application to finite element methods

Ngoc Cuong Nguyen^a, Jordi Vila-Pérez^a, Jaime Peraire^a

^a*Center for Computational Engineering, Department of Aeronautics and Astronautics, Massachusetts Institute of Technology, 77 Massachusetts Avenue, Cambridge, MA, 02139, USA*

Abstract

We introduce an adaptive viscosity regularization approach for the numerical solution of systems of nonlinear conservation laws with shock waves. The approach seeks to solve a sequence of regularized problems consisting of the system of conservation laws and an additional Helmholtz equation for the artificial viscosity. We propose a homotopy continuation of the regularization parameters to minimize the amount of artificial viscosity subject to positivity-preserving and smoothness constraints on the numerical solution. The regularization methodology is combined with a mesh adaptation strategy that identifies the shock location and generates shock-aligned meshes, which allows to further reduce the amount of artificial dissipation and capture shocks with increased accuracy. We use the hybridizable discontinuous Galerkin method to numerically solve the regularized system of conservation laws and the continuous Galerkin method to solve the Helmholtz equation for the artificial viscosity. We show that the approach can produce approximate solutions that converge to the exact solution of the Burgers' equation. Finally, we demonstrate the performance of the method on inviscid transonic, supersonic, hypersonic flows in two dimensions. The approach is found to be accurate, robust and efficient, and yields very sharp yet smooth solutions in a few homotopy iterations.

Keywords: conservation laws, shock waves, shock capturing, adaptive viscosity, discontinuous Galerkin methods, finite element methods

1. Introduction

The formation of shock waves is one of the most challenging problems in numerical approximation of nonlinear conservation laws. Difficulties in capturing shock waves are that (1) at the very moment a shock is formed it poses a source of instability in the shock region, which then leads to numerical instabilities if no treatment of shock waves is introduced; (2) it is hard to predict when and where new shocks arise, and track them as they propagate through the physical domain and interact with each other and with boundary layers and vortices; and (3) numerical treatment of shock waves should not cause deterioration in resolution and reduction of accuracy in domains where the solution is smooth. For high-order numerical methods, insufficient resolution or an inadequate treatment of shocks can result in Gibbs oscillations, which grow rapidly and contribute to numerical instabilities. These challenges have been a driving force behind the development of shock capturing methods designed to detect and stabilize shocks.

A number of shock detection methods rely on the non-smoothness of the numerical solution to detect shocks as well as other sharp features [1, 2, 3, 4, 5, 6, 7, 8, 9, 10, 11]. Among them, the sensor by [7], devised in the context of DG methods, takes advantage of the theoretical convergence rate of DG schemes for smooth solutions in order to detect discontinuities. The shock sensor by [10, 11] is based on the decay rate of the coefficients of the DG polynomial approximation. Other methods that rely on high-order derivatives of the solution include [1, 2, 3, 4, 5, 6, 8, 9, 12, 13], and apply to numerical schemes for which such derivatives can be computed, such as spectral methods and finite difference methods. The most simple shock-detection method is to take advantage of the strong compression that a fluid undergoes across a shock wave and use the divergence of the velocity field as a shock sensor [14, 15, 16].

Shock stabilization methods lie within one of the following two categories: limiters and artificial viscosity. Limiters, in the form of flux limiters [17, 18, 19], slope limiters [20, 7, 21, 22], and WENO-type schemes [23, 24, 25, 26] pose implementation difficulties for implicit time integration schemes and high-order methods on complex geometries. As for artificial viscosity methods, Laplacian-based [27, 28, 29, 15, 16, 10, 11] and physics-based [30, 31, 1, 2, 14, 3, 4, 5, 8, 9, 10] approaches have been proposed. An assessment of artificial viscosity methods for LES is presented in [32].

Shock capturing using artificial viscosity may date back as early as 1950 [33].

The main idea is to add an artificial viscous term into the governing equations to stabilize shock waves without affecting the solution away from the shock region. When the amount of viscosity is properly added in a neighborhood of shocks, the solution can converge uniformly except in the region around shocks, where it is smoothed and spread out over some length scale. On the other hand, excessive addition of artificial viscosity may negatively affect the computed solution not only in the shock region but also in other parts of the domain where the solution is smooth. Artificial viscosity has been widely used in finite volume methods [34], streamline upwind Petrov-Galerkin (SUPG) methods [35], spectral methods [36, 37], as well as DG methods [27, 38, 39, 10, 40, 41]. Both Laplacian-based [28, 29, 16, 15, 10, 11] and physics-based [30, 42, 8, 2, 43, 3, 4, 5, 9, 44] artificial viscosity methods have been used for shock capturing.

The recent work [45, 46, 47] introduces an optimization-based method for resolving discontinuous solutions of conservation laws with high-order numerical discretizations that support inter-element solution discontinuities, such as discontinuous Galerkin or finite volume methods [46]. The method aims to align inter-element boundaries with discontinuities in the solution by deforming the computational mesh in order to avoid Gibbs' phenomena. It requires solution of a PDE-constrained optimization problem for both the computational mesh and the numerical solution using sequential quadratic programming solver. Recently, a moving discontinuous Galerkin finite element method with interface condition enforcement (MDG-ICE) [48, 49, 50] is formulated for shock flows by enforcing the interface condition separately from the conservation laws. In the MDG-ICE method, the discrete grid geometry is treated as an additional variable to detect interfaces and satisfy the interface condition, thereby directly fitting shocks and preserving high-order accurate solutions. The Levenberg-Marquardt method is used to solve the regularized coupled system of the conservation laws and the interface condition to obtain the approximate solution and the shock-aligned mesh.

In this paper, we introduce an adaptive viscosity regularization approach for the numerical solution of nonlinear conservation laws with shock waves. The approach aims to numerically solve a sequence of viscosity-regularized problems by making the amount of viscosity as small as possible while simultaneously enforcing relevant physics and smoothness constraints on the numerical solution. The methodology is based on two main ingredients: the viscosity regularization of nonlinear conservation laws and the homotopy continuation of regularization parameters. In particular, the viscosity regulariza-

tion consists of a PDE-based artificial viscosity method [27, 38] which couples the regularized conservation laws with an additional Helmholtz equation for the artificial viscosity. On the other hand, homotopy continuation is used to minimize the amount of artificial viscosity subject to positivity-preserving and smoothness constraints on the numerical solution. We propose a relaxation variant of our method to solve the regularized conservation laws and the Helmholtz equation separately.

The presented approach is general and minimizes the amount of artificial viscosity needed for stabilizing the numerical solution under the presence of shocks on a given mesh. Nevertheless, this strategy can be coupled to mesh adaptation algorithms that identify the shock location and generate a shock-aligned grid in order to further reduce the amount of artificial dissipation. To this end, we also introduce an algorithm to locate shock waves and generate shock-aligned meshes so as to reduce considerably the amount of artificial viscosity and approximate the exact solution of the original conservation laws with increased accuracy.

Whereas different numerical schemes, such as finite volume methods and finite difference methods, can be used to discretize the governing equations, this paper employs finite element methods. In particular, we use the hybridizable discontinuous Galerkin (HDG) method [51, 52, 53, 54, 41, 55, 56, 57, 58] to numerically solve the viscosity-regularized conservation laws and the continuous Galerkin (CG) method to solve the Helmholtz equation for the artificial viscosity. The HDG method is considered here due to its efficiency and high-order accuracy, while the CG method is employed to provide a continuous viscosity field. The continuity and smoothness of the artificial viscosity is highly desirable [27, 15, 40, 38]. We demonstrate the approach on inviscid transonic, supersonic, hypersonic flows in two dimensions. The approach is found to be efficient and robust enough that it does not require continuation in time for steady-state problems, so solution convergence can be reached in a few number of iterations.

The paper is organized as follows. We present the adaptive viscosity regularization approach in Section 2, which is accompanied by the description of the homotopy continuation procedure, the specification of the physical and numerical constraints, and the proposed shock identification and mesh alignment algorithms. Next, in Section 3, we describe the numerical approximation of the governing equations by using a combination of the hybridizable discontinuous Galerkin method and the continuous Galerkin method. In Section 4, we present numerical results to assess the performance of the proposed

approach on the inviscid Burgers' equation and inviscid transonic, supersonic, and hypersonic flows. Finally, in Section 5, we conclude the paper with some remarks and future work.

2. Adaptive Viscosity Regularization Approach

2.1. Viscosity regularization of nonlinear hyperbolic systems

We consider a hyperbolic system of m conservation laws, defined on the physical domain $\Omega \in \mathbb{R}^d$ and subject to appropriate initial and boundary conditions, as follows

$$\frac{\partial \mathbf{u}}{\partial t} + \nabla \cdot \mathbf{F}(\mathbf{u}) = 0 \quad \text{in } \Omega, \quad (1)$$

where $\mathbf{u}(\mathbf{x}) \in \mathbb{R}^m$ is the solution of the system of conservation laws at $\mathbf{x} \in \Omega$ and the physical fluxes $\mathbf{F} = (\mathbf{f}_1(\mathbf{u}), \dots, \mathbf{f}_d(\mathbf{u})) \in \mathbb{R}^{m \times d}$ include d vector-valued functions of the solution. We assume that the fluxes \mathbf{F} are smooth functions of \mathbf{u} and that the system is hyperbolic in the sense that the Jacobian matrix $\mathbf{A}(\mathbf{u}) = \sum_{i=1}^d \alpha_i \partial \mathbf{f}_i(\mathbf{u}) / \partial \mathbf{u}$ has real eigenvalues and is diagonalizable for all $\alpha_1, \dots, \alpha_d \in \mathbb{R}$. Furthermore, we assume that (1) is a non-dimensional system.

A distinguished feature of nonlinear hyperbolic systems is the possible development of shock waves in the exact solution even if the initial data is smooth. Shock waves have always been a considerable source of difficulties toward a rigorous mathematical treatment of nonlinear hyperbolic systems. In the presence of shock waves, the system of conservation laws (1) admits a class of weak solutions in a distributional sense [59]. In order to single out the unique ‘‘physically relevant’’ solution among all possible weak solutions, additional entropy conditions must be imposed along shocks [37]. The unique entropic solutions of the hyperbolic system (1) coincide with the vanishing viscosity solutions of the following parabolic system

$$\frac{\partial \mathbf{u}}{\partial t} + \nabla \cdot \mathbf{F}(\mathbf{u}) - \nabla \cdot \varepsilon \nabla \mathbf{u} = 0 \quad \text{in } \Omega, \quad (2)$$

in the limit of the vanishing viscosity $\varepsilon \rightarrow 0$ [59]. The parabolic system (2) is a viscosity regularization of the original hyperbolic system (1) and results in the artificial viscosity method for capturing shock waves.

Herein we follow [27, 38] to consider a more sophisticated viscosity regularization of the original hyperbolic system (1) as follows

$$\frac{\partial \mathbf{u}}{\partial t} + \nabla \cdot \mathbf{F}(\mathbf{u}) - \lambda \nabla \cdot \mathbf{G}(\mathbf{u}, \nabla \mathbf{u}, \eta) = 0 \quad \text{in } \Omega, \quad (3a)$$

$$\eta - \kappa^2 \nabla \cdot (\ell^2 \nabla \eta) - s(\mathbf{u}, \nabla \mathbf{u}) = 0 \quad \text{in } \Omega, \quad (3b)$$

where $\eta(\mathbf{x})$ is the solution of the Helmholtz equation (3b) with homogeneous Neumann boundary conditions

$$\eta = 0 \quad \text{on } \Gamma_{\text{wall}}, \quad \ell^2 \nabla \eta \cdot \mathbf{n} = 0 \quad \text{on } \partial\Omega \setminus \Gamma_{\text{wall}}, \quad (4)$$

with Γ_{wall} being the wall boundary. Here λ is the first regularization parameter that controls the amplitude of artificial viscosity, and κ is the second regularization parameter that controls the thickness of artificial viscosity. Furthermore, ℓ is an appropriate length scale.

The source term s in (3b) is required to determine η . It must meet several requirements in order to yield an effective artificial viscosity. First and foremost, it must be a non-negative function. Second, it takes positive value in the shock region and smoothly vanishes to zero away from the shock region. Third, the positive value of the source term is proportional to the shock strength. And last, it must be a smooth function of \mathbf{u} and $\nabla \mathbf{u}$. The source term should depend on the solution gradient because gradient information is needed to determine the shock strength. A particular source term that satisfies the above requirements is defined as follows

$$s(\mathbf{u}, \nabla \mathbf{u}) = g(S) \quad (5)$$

where $g(S)$ is a smooth approximation of the following step function

$$\tilde{g}(S) = \begin{cases} 0 & \text{if } S < 0, \\ S & \text{if } 0 \leq S \leq s_{\text{max}}, \\ s_{\text{max}} & \text{if } S > s_{\text{max}}, \end{cases} \quad (6)$$

and the quantity S is a measure of the shock strength which is in this paper given by

$$S(\mathbf{u}, \nabla \mathbf{u}) = -\nabla \cdot \mathbf{v}. \quad (7)$$

Here \mathbf{v} is the non-dimensional velocity field that is determined from the state vector \mathbf{u} . The parameter s_{max} is used to put an upper bound on the

source term when the divergence of the velocity becomes too negatively large. Herein we choose $s_{\max} = 0.5\|S\|_{\infty}$, where $\|S\|_{\infty} = \max_{\mathbf{x} \in \Omega} |S(\mathbf{x})|$ is the L_{∞} norm. Figure 1 shows $g(S)$ and $\tilde{g}(S)$ as a function of S . The source term is only active in the region of the flow where the divergence of the velocity field is negative. The use of the velocity divergence as shock strength for defining an artificial viscosity field has appeared in [14, 15, 16].

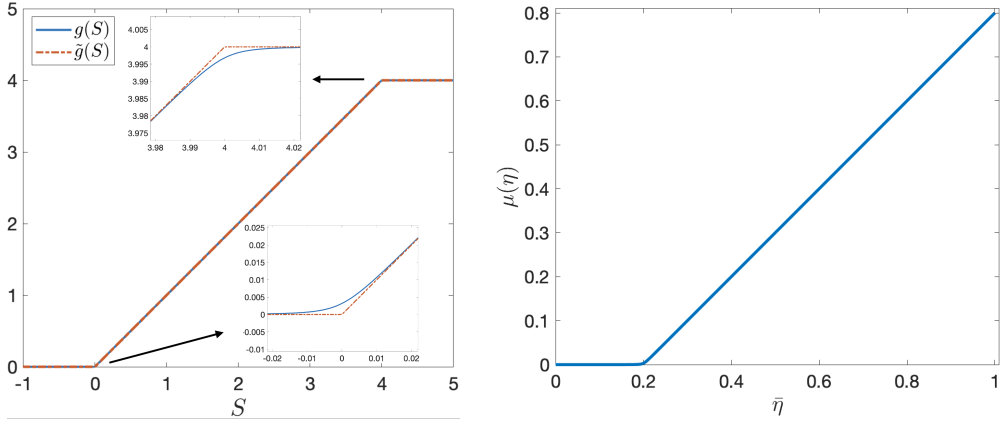


Figure 1: The source term s as a function of the shock strength S for $s_{\max} = 4$ (left) and the artificial viscosity $\mu(\eta)$ as a function of $\bar{\eta}$ for $\eta_0 = 0.2$ (right). Note that the derivative of $g(S)$ is continuous at $S = 0$ and $S = s_{\max}$, whereas that of $\tilde{g}(S)$ is discontinuous there.

The artificial fluxes \mathbf{G} provide a viscosity regularization to smooth out the discontinuities in the exact solution of the original hyperbolic system. With a proper choice of the artificial fluxes, the solution \mathbf{u} of the regularized system (3a) must be continuous for positive values of λ and η . There are a number of different options for the artificial fluxes \mathbf{G} . In this paper, we use the Laplacian fluxes of the form

$$\mathbf{G}(\mathbf{u}, \nabla \mathbf{u}, \eta) = \mu(\eta) \nabla \mathbf{u}, \quad (8)$$

where

$$\mu(\eta) = (\bar{\eta} - \eta_0) \left(\frac{\arctan(100(\bar{\eta} - \eta_0))}{\pi} + \frac{1}{2} \right) - \frac{\arctan(100)}{\pi} + \frac{1}{2} \quad (9)$$

is a smooth approximation of a ramp function as shown in Figure 1. Here $\bar{\eta} = \eta/\|\eta\|_{\infty}$ is the normalized function with $\|\eta\|_{\infty} = \max_{\mathbf{x} \in \Omega} |\eta(\mathbf{x})|$ being the L_{∞} norm. Note that η_0 is the artificial viscosity threshold that makes

$\mu(\eta)$ vanish to zero when $\bar{\eta} \leq \eta_0$. In other words, artificial viscosity is only added to the shock region where $\bar{\eta}$ exceeds η_0 . Therefore, the threshold η_0 will help remove excessive artificial viscosity. Since $\|\bar{\eta}\|_\infty = 1$, $\eta_0 = 0.2$ is a sensible choice. Note that the artificial viscosity field $\varepsilon(\mathbf{x})$ is equal to $\lambda\mu(\mathbf{x})$, where $\mu(\mathbf{x})$ is bounded by $\mu(\mathbf{x}) \in [0, 1 - \eta_0]$ for any $\mathbf{x} \in \Omega$. We can also consider a more general form $\mathbf{G} = \mu(\eta)\nabla\mathbf{u}^*$ [27, 16], where \mathbf{u}^* is a modified state vector. Both are known as Laplacian-based artificial viscosity. Another option is physics-based artificial viscosity by taking \mathbf{G} to be the viscous stress tensor and the heat flux of the Navier-Sokes equation and adding the artificial viscosity to the physical viscosities and thermal conductivity [60, 61].

We still need to determine λ and κ in order to close the system (3). If λ is too small, then ε will not be large enough to stabilize the numerical method used to solve the system (3). But if λ is too large, then the solution of the system (3) will be no longer an accurate approximation to the solution of the original system (1). Likewise, if κ is too small, then ε will not be sufficiently smooth to stabilize the numerical method used to solve the system (3). But if κ is too large, then the solution of the system (3) will be no longer an accurate approximation to the solution of the original system (1) since ε spreads out beyond the shock region.

2.2. Homotopy continuation of the regularization parameters

In this paper we will focus on steady-state problems. We describe the adaptive regularization approach for numerically solving the steady-state version of the nonlinear hyperbolic system. In this case, the coupled system (3) reduces to

$$\nabla \cdot \mathbf{F}(\mathbf{u}) - \lambda \nabla \cdot \mathbf{G}(\mathbf{u}, \nabla \mathbf{u}, \eta) = 0 \quad \text{in } \Omega, \quad (10a)$$

$$\eta - \kappa^2 \nabla \cdot (\ell \nabla \eta) - s(\mathbf{u}, \nabla \mathbf{u}) = 0 \quad \text{in } \Omega. \quad (10b)$$

For time-dependent problems, the same approach can be applied to the fully discrete system at every time step.

We denote by \mathcal{T}_h a collection of curved elements that partition the physical domain Ω . For any element $K \in \mathcal{T}_h$, we say that it belongs to the shock region if the following inequality holds

$$\frac{\int_K \bar{\eta} d\mathbf{x}}{\int_K d\mathbf{x}} \geq \eta_0 \quad (11)$$

where $\bar{\eta} = \eta/\|\eta\|_\infty$. The left quantity is the cell average of the shock strength measure. The shock region is defined by

$$\mathcal{T}_h^{\text{shock}} = \{K \in \mathcal{T}_h : \int_K \bar{\eta} d\mathbf{x} \geq \eta_0|K|\}. \quad (12)$$

We choose $\ell = h_{\min}$, where h_{\min} is the smallest edge over all elements in the shock region. This choice is made because we would like the artificial viscosity to concentrate along the shock. In this case, the parameter κ must satisfy $\kappa \geq 1$ because the artificial viscosity will not be smooth enough to stabilize the numerical solution if $\kappa < 1$ when $\ell = h_{\min}$.

The pair of regularization parameters (λ, κ) controls the magnitude and thickness of the artificial viscosity in order to obtain accurate solutions. On the one hand, if (λ, κ) is too small then the numerical solution can develop oscillations across the shock waves. On the other hand, if (λ, κ) is too large the solution becomes less accurate in the shock region, which in turn affects the accuracy of the solution in the remaining region. Therefore, we propose a homotopy continuation method to determine (λ, κ) . The key idea is to solve the regularized system with a large value of (λ, κ) first and then gradually decrease (λ, κ) until any of the physics or smoothness constraints on the numerical solution are violated. At this point, we take the value of (λ, κ) from the previous iteration where the numerical solution still satisfies all of the physics and smoothness constraints. This procedure is summarized in the following algorithm:

- Given initial value (λ_0, κ_0) , numerically solve the coupled system (10) with $(\lambda, \kappa) = (\lambda_0, \kappa_0)$ to obtain the initial solution (\mathbf{u}_0, η_0) .
- Set $\lambda_n = \zeta^n \lambda_0$ and $\kappa_n = 1 + \zeta^n (\kappa_0 - 1)$ for some constant $\zeta \in (0, 1)$ and solve the coupled system (10) with $(\lambda, \kappa) = (\lambda_n, \kappa_n)$ to obtain the iterative solution (\mathbf{u}_n, η_n) for $n = 1, 2, \dots$ until \mathbf{u}_n violates any of the constraints.
- Finally, we accept \mathbf{u}_{n-1} as the numerical solution of the original system of conservation laws.

The adaptive viscosity regularization approach can be seen as a method

to solve the following minimization problem

$$\min_{\lambda \in \mathbb{R}^+, \kappa \geq 1, \mathbf{u}, \eta} \lambda \kappa \quad (13a)$$

$$\text{s.t. } \mathcal{L}(\mathbf{u}, \eta, \lambda, \kappa) = 0 \quad (13b)$$

$$\mathbf{u} \in \mathcal{C}. \quad (13c)$$

Here \mathcal{L} represents the spatial discretization of the coupled system (10) by a numerical method and \mathcal{C} represents a set of constraints on the numerical solution. The objective function is to minimize the amount of artificial viscosity which is proportional to $\lambda\kappa$. The constraints rule out unwanted solutions of the discrete system (13b) and play an important role in yielding a high-quality numerical solution. Hence, the optimization problem (13) is to minimize the amount of artificial viscosity while ensuring the physicality and accuracy of the numerical solution. We will later introduce the constraints that are used to obtain such numerical solution.

2.3. Relaxation variant of the adaptive viscosity regularization

The above homotopy continuation method requires us to solve the coupled system (10). In order to be able to decouple the system (10), we propose the following variant of the homotopy continuation:

- Given an initial choice of (λ_0, κ_0) and η_0 such that $\|\eta_0\|_\infty = 1$, solve the regularized system (10a) with $\lambda = \lambda_0, \eta = \eta_0$ to obtain the initial solution \mathbf{u}_0 .
- Set $\lambda_n = \zeta^{n-1} \lambda_{n-1}$ and $\kappa_n = 1 + \zeta^{n-1}(\kappa_{n-1} - 1)$ for some constant $\zeta \in (0, 1)$; solve the Helmholtz equation (10b) with $\kappa = \kappa_n$ and the source term from \mathbf{u}_{n-1} to obtain η_n and normalize $\eta_n = \eta_n / \|\eta_n\|_\infty$; and solve the regularized system (10a) with $\lambda = \lambda_n, \eta = \eta_n$ to obtain the iterative solution \mathbf{u}_n for $n = 1, 2, \dots$ until \mathbf{u}_n violates any of the constraints.
- Finally, we accept \mathbf{u}_{n-1} as the numerical solution of the system of conservation laws.

The initial function η_0 can be set to 1 on most of the physical domain Ω except near the wall boundary where it vanishes smoothly to zero at the wall. The initial value λ_0 is conservatively large to make the initial solution

\mathbf{u}_0 very smooth (but it is usually not an accurate solution). The initial value κ_0 depends on the type of meshes used to compute the numerical solution. For regular meshes that have the elements of the same size in the shock region, $\kappa_0 = 1.5$ is a sensible choice. For adaptive meshes that are refined toward the shock region, we choose $\kappa_0 = 5$ since $\ell = h_{\min}$ is extremely small for shock-adaptive meshes. In any case, κ_n will decrease from κ_0 toward 1 during the homotopy iteration. Hence, the choice of κ_0 can be flexible.

Unlike the previous homotopy procedure, this procedure solves the Helmholtz equation (10b) separately from the regularized system (10a). Hence, different numerical methods can be used to solve (10a) and (10b) separately. Indeed, we use the hybridizable discontinuous Galerkin (HDG) method to solve (10a) and the continuous Galerkin (CG) method to solve (10b) for the numerical experiments presented in Section 4. The CG method is used to solve (10b) instead of the HDG method mainly because we prefer the artificial viscosity field to be continuous.

The relaxation variant of our approach is robust enough that we do not need to use continuation in time and polynomial degree even when we start the homotopy process from the freestream flow. Furthermore, the number of homotopy iterations required to reach the converged solution is usually around 10. The present approach is a robust and efficient shock capturing method for the numerical solution of conservation laws with shock waves.

2.4. Solution constraints

The physical constraints are that pressure and density must be positive. In order to establish a smoothness constraint on the numerical solution, we express an approximate scalar variable ξ of degree k within each element in terms of an orthogonal basis and its truncated expansion of degree $k - 1$ as

$$\xi = \sum_{i=1}^{N(k)} \xi_i \psi_i, \quad \xi^* = \sum_{i=1}^{N(k-1)} \xi_i \psi_i \quad (14)$$

where $N(k)$ is the total number of terms in the k -degree expansion and ψ_i are the basis functions [10]. In this paper, ξ is chosen to be either density or pressure when we use the method to solve the Euler equations. For scalar conservation laws, ξ is the numerical solution. We introduce the following quantity

$$\sigma(\lambda_n, \kappa_n) = \max_{K \in \mathcal{T}_h^{\text{shock}}} \sigma_K(\lambda_n, \kappa_n), \quad \sigma_K(\lambda_n, \kappa_n) \equiv \frac{\int_K |\xi_n / \xi_n^* - 1| d\mathbf{x}}{\int_K d\mathbf{x}}. \quad (15)$$

Some shock capturing methods [10, 38] use a piecewise-constant function similar to σ_K in (15) to compute the artificial viscosity field. Herein we employ this type of functions to devise a smoothness constraint on the numerical solution as follows.

When λ_n, κ_n are sufficiently large at the beginning of the homotopy loop, we expect $\sigma(\lambda_n, \kappa_n)$ to be small. As we gradually decrease λ_n, κ_n during the homotopy continuation, we expect $\sigma(\lambda_n, \kappa_n)$ to increase. Figure 2 illustrates this behavior of $\sigma(\lambda_n, \kappa_n)$ for the inviscid hypersonic flow past a circular cylinder at $M_\infty = 7$. It is important to note that $\sigma(\lambda_n, \kappa_n)$ depends on ξ , being this term either density or pressure. Indeed, $\sigma(\lambda_n, \kappa_n)$ is about 10 times larger when ξ is chosen to be density instead of pressure. However, note that the ratio $\sigma(\lambda_n, \kappa_n)/\sigma(\lambda_1, \kappa_1)$ behaves very similarly in both cases. Finally, since we would like to bound $\sigma(\lambda_n, \kappa_n)$ because the numerical solution will be oscillatory if $\sigma(\lambda_n, \kappa_n)$ exceeds a certain value, we impose a bound on the ratio $\sigma(\lambda_n, \kappa_n)/\sigma(\lambda_1, \kappa_1)$. Hence, we introduce the following smoothness constraint

$$\frac{\sigma(\lambda_n, \kappa_n)}{\sigma(\lambda_1, \kappa_1)} \leq C_\sigma, \quad (16)$$

where $C_\sigma > 1$ is a smoothness parameter that controls the smoothness of the numerical solution. Figure 3 shows the approximate density and pressure along $y = 0$ for the inviscid hypersonic flow pas a cylinder. While the approximate solution is sharper and more accurate as $\sigma(\lambda_n, \kappa_n)/\sigma(\lambda_1, \kappa_1)$ increases, it becomes oscillatory when $\sigma(\lambda_n, \kappa_n)/\sigma(\lambda_1, \kappa_1)$ exceeds 10. A reasonably conservative choice for the smoothness parameter is $C_\sigma = 5$.

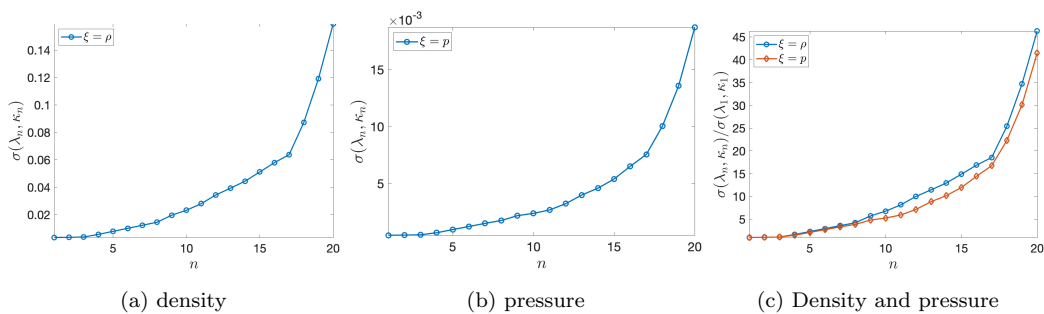


Figure 2: The computed value of $\sigma(\lambda_n, \kappa_n)$ as we gradually decrease (λ_n, κ_n) in the homotopy continuation for the inviscid hypersonic flow past a circular cylinder at $M_\infty = 7$ on a regular mesh: (a) ξ is chosen to be density, (b) ξ is chosen to be pressure, (c) the normalized function $\sigma(\lambda_n, \kappa_n)/\sigma(\lambda_1, \kappa_1)$ for both cases.

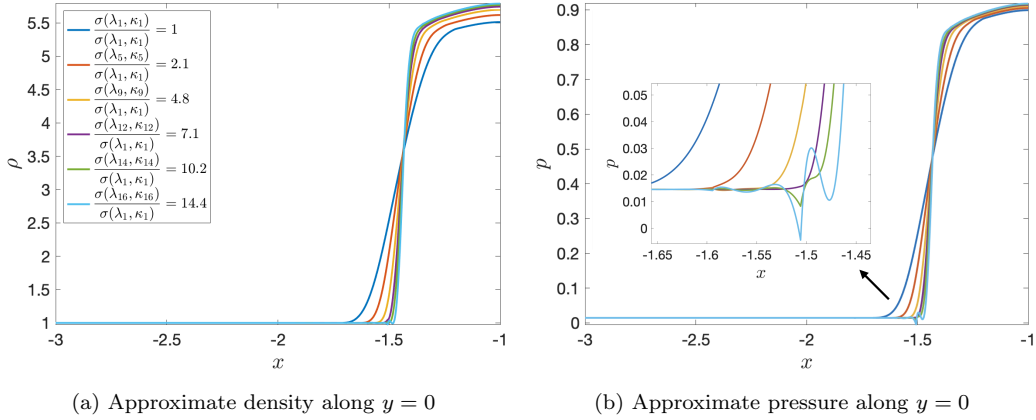


Figure 3: The plot of the approximate density and pressure along the horizontal line $y = 0$ for several values of $\sigma(\lambda_n, \kappa_n)/\sigma(\lambda_1, \kappa_1)$ for the inviscid hypersonic flow past a cylinder at $M_\infty = 7$ on a regular mesh. The approximate density is sharper and more accurate as $\sigma(\lambda_n, \kappa_n)/\sigma(\lambda_1, \kappa_1)$ increases during the homotopy continuation. The approximate pressure is smooth for $\sigma(\lambda_n, \kappa_n)/\sigma(\lambda_1, \kappa_1) \leq 7.1$, mildly oscillatory for $\sigma(\lambda_n, \kappa_n)/\sigma(\lambda_1, \kappa_1) = 10.2$, and oscillatory and negative for $\sigma(\lambda_n, \kappa_n)/\sigma(\lambda_1, \kappa_1) = 14.4$.

It is important to choose a sufficiently large value for (λ_0, κ_0) , so that $\sigma(\lambda_n, \kappa_n)$ slowly increases when (λ_n, κ_n) gradually decreases for the first few homotopy iterations. A rapid increase of $\sigma(\lambda_n, \kappa_n)$ for the first few homotopy iterations should not be allowed, because it is likely to result in oscillatory solutions. If this is encountered, it is likely that (λ_0, κ_0) is not large enough and a larger value for (λ_0, κ_0) must be used. It is completely acceptable for $\sigma(\lambda_n, \kappa_n)$ to decrease during the first few homotopy iterations. If this occurs, we replace the smoothness constraint (16) with

$$\frac{\sigma(\lambda_n, \kappa_n)}{\sigma(\lambda_m, \kappa_m)} \leq C_\sigma, \quad (17)$$

where $m = \arg \min_{k \in [1, 2, \dots, n-1]} \sigma(\lambda_k, \kappa_k)$. In other words, $\sigma(\lambda_m, \kappa_m)$ is the smallest value of $\sigma(\lambda_k, \kappa_k)$ for $k = 1, \dots, n-1$, during the homotopy continuation loop.

The physical constraints ensure that the integral in (15) is bounded since both ξ_n and ξ_n^* are positive. For scalar conservation laws, there may be no such constraints and it is possible for ξ_n and ξ_n^* to be zero. In that case, we suggest to replace ξ_n/ξ_n^* with 1 whenever ξ_n^* is zero or very close to zero. For the Euler equations, the constraint set \mathcal{C} in (13) consists of the following

constraints

$$\rho(\mathbf{x}) > 0, \quad p(\mathbf{x}) > 0, \quad \frac{\sigma(\lambda_n, \kappa_n)}{\sigma(\lambda_m, \kappa_m)} \leq C_\sigma. \quad (18)$$

The first two constraints enforce the positivity of density and pressure, while the last constraint guarantees the smoothness of the numerical solution. The smoothness constraint indirectly imposes a degree of regularity on the numerical solution. It plays a vital role in making the homotopy continuation method so robust that there is no need for continuation in time or polynomial degree to obtain the numerical solution.

2.5. Mesh sensitivity: shock-aligned grid generation

The proposed adaptive regularization approach is a general procedure that is able to provide the optimal artificial viscosity for any kind of mesh. Nevertheless, it is important to remark that the artificial dissipation field depends on the grid \mathcal{T}_h . Meshes that are aligned and refined along the shock allow a significant reduction of the artificial viscosity λ , which leads to sharper and more accurate approximations. In this study, we will compare the performance of the viscosity regularization procedure for both uniform and shock-aligned grids. In particular, we introduce a mesh adaptation procedure that identifies the shock location based on the solution on the uniform grid and constructs a new mesh that is aligned and refined along the approximated shock location, as described throughout this section.

Note that this process could be iterated successively until no artificial viscosity was required, leading to a robust shock-alignment strategy that renders the exact solution of the original system of conservation laws. Nevertheless, since the aim of this work focuses on introducing an adaptive regularization approach that can be used with any mesh, the so-called shock-aligned meshes that we will employ in the numerical studies will consist of a single shock adaptation iteration.

2.5.1. Identifying the shock location

A shock can be represented by a curve in two dimensions or a surface in three dimensions. There can be several shocks that exist in the physical domain. We propose a method to construct curves or surfaces to represent possible shocks in the physical domain. The idea is to use the normalized shock indicator $\bar{\eta}(\mathbf{x})$ to find a set of faces and construct shock curves/surfaces from those faces. The method can be described as follows:

- Find the shock region $\mathcal{T}_h^{\text{shock}} = \{K \in \mathcal{T}_h : \int_K \bar{\eta}(\mathbf{x}) d\mathbf{x} \geq \eta_0 |K|\}$.
- Map a set of points on the reference element K_{ref} to a set of points on a physical element K for all $K \in \mathcal{T}_h^{\text{shock}}$. The total number of points in the shock region is equal to $N_s \times N_p$, where N_s is the number of elements in the shock region and N_p is the number of points on the reference element.
- Select only the points in the shock region that satisfy $\bar{\eta}(\mathbf{x}) \geq 2\eta_0$.
- Determine M bounding boxes $\{\mathcal{B}\}_{m=1}^M$ that contain the selected points. M should be chosen large enough to map the shock curves/surfaces accurately.
- For every edge L_{mj} of each bounding box \mathcal{B}_m along the freestream velocity direction, find $\mathbf{x}_{mj} = \arg \max_{\mathbf{x} \in L_{mj}} \bar{\eta}(\mathbf{x})$ for $j = 1, \dots, 2^{d-1}$. Each bounding box \mathcal{B}_m contains two points $\mathbf{x}_{m1}, \mathbf{x}_{m2}$ in two dimensions, or four points $\mathbf{x}_{m1}, \mathbf{x}_{m2}, \mathbf{x}_{m3}, \mathbf{x}_{m4}$ in three dimensions. Let \mathcal{F}_m be a face formed by $\{\mathbf{x}_{mj}\}_{j=1}^{2^{d-1}}$ for each bounding box \mathcal{B}_m .
- The shock location is determined by the set of M faces $\{\mathcal{F}_m\}_{m=1}^M$. This set may contain a number of disjoint subsets of connected faces. Each disjoint subset of connected faces represents one shock curve/surface. Hence, the number of shocks in the physical domain is equal to the number of disjoint subsets of connected faces.

The shock identification procedure is illustrated in Figure 4(a) for inviscid transonic flows past NACA 0012 airfoil, where there are an upper (strong) shock and a lower (weak) shock. As a result, the procedure yields two disjoint subsets of connected faces.

2.5.2. Generating shock-aligned meshes

Having identified the shock location, we generate shock-aligned meshes to substantially reduce the regularization parameter and improve the numerical solution in the shock region. The mesh generation method can be described as follows:

- Polynomial interpolation is used to fit each disjoint subset of connected faces to obtain a smooth shock curve.

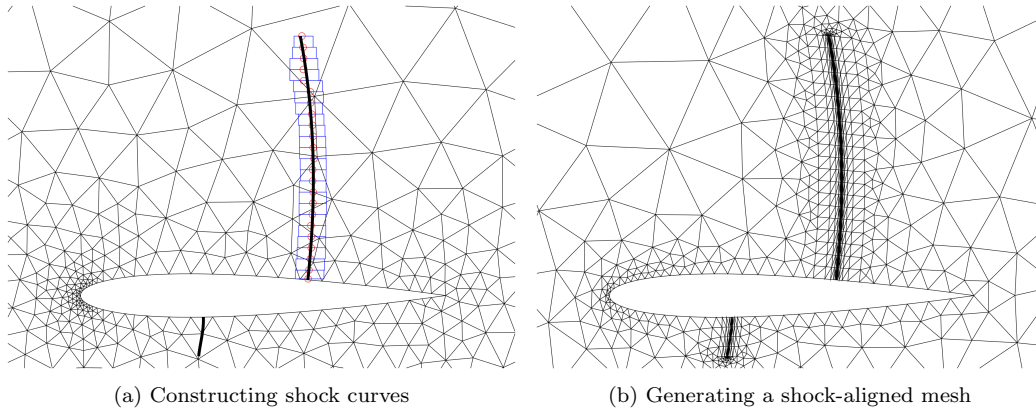


Figure 4: Identification of shock curves (a) and construction of a shock-aligned mesh for inviscid transonic flow past the NACA 0012 airfoil at $M_\infty = 0.8$ and 1.5° angle of attack.

- Next, create a grid of N nodes and M faces for the shock curve. For high-order methods, the grid should be made high-order to represent the shock curve accurately.
- Extrude each node on the shock curve along a specified direction to create a number of new nodes. Typically, the direction is the normal vector at the node. However, if the shock curve intersects with the domain boundary, different directions can be chosen to make the mesh conform to the domain boundary. Furthermore, the directions behind the shock curve can also be different from the directions before the shock curve.
- Connect the nodes on the shock curve and the newly created nodes to form a shock-aligned mesh based on the grid of the shock curve.
- Repeat the above steps for the remaining disjoint subsets of connected faces to generate their shock-aligned meshes.
- Finally, generate a mesh for the remaining region of the physical domain and connect this mesh with the shock-aligned meshes to obtain a full mesh for the entire physical domain.

The mesh generation is illustrated in Figure 4(b). We use Gmsh [62] to generate meshes for the smooth region of the physical domain. This is done by collecting the mesh points on the boundary of the shock-aligned meshes

together with the points on the boundary of the physical domain to define a geometry description of the smooth region.

3. Application to Finite Element Methods

In the adaptive viscosity regularization approach described in Section 2, one can use any appropriate numerical method to solve the viscosity-regularized conservation laws and the Helmholtz equation. In this paper, we employ a discontinuous Galerkin (DG) method to solve the former and the continuous Galerkin (CG) method to solve the latter. We use the CG method since it allows us to obtain a continuous artificial viscosity field. The HDG method [51, 52, 53, 54, 41, 55, 56, 57, 58] is well-suited for solving the regularized conservation laws because of its efficiency and high-order accuracy.

3.1. Hybridizable discontinuous Galerkin method

We briefly describe the HDG method for solving the following problem

$$\nabla \cdot \mathbf{F}(\mathbf{u}) - \lambda \nabla \cdot \mathbf{G}(\mathbf{u}, \nabla \mathbf{u}, \eta) = 0 \quad \text{in } \Omega, \quad (19)$$

subject to appropriate boundary conditions on $\partial\Omega$, when both λ and η are known. We denote by $\partial\mathcal{T}_h$ the set $\{\partial K : K \in \mathcal{T}_h\}$, that is, a collection of the boundaries of all elements in \mathcal{T}_h . We shall denote by \mathbf{n} the outward unit normal of ∂K . For an element K of the collection \mathcal{T}_h , $F = \partial K \cap \partial\Omega$ is the boundary face if the $d - 1$ Lebesgue measure of F is nonzero. For two elements K^+ and K^- of the collection \mathcal{T}_h , $F = \partial K^+ \cap \partial K^-$ is the interior face between K^+ and K^- if the $d - 1$ Lebesgue measure of F is nonzero. We denote by \mathcal{E}_h the set of all faces in \mathcal{T}_h . Let $\mathcal{P}^k(D)$ denote the set of polynomials of degree at most k on a domain D . We introduce discontinuous finite element spaces

$$\begin{aligned} \mathcal{V}_h^k &= \{\mathbf{a} \in (L^2(\mathcal{T}_h))^m : \mathbf{a}|_K \in (\mathcal{P}^k(K))^m, \forall K \in \mathcal{T}_h\}, \\ \mathcal{Q}_h^k &= \{\mathbf{A} \in (L^2(\mathcal{T}_h))^{m \times d} : \mathbf{A}|_K \in (\mathcal{P}^k(K))^{m \times d}, \forall K \in \mathcal{T}_h\}, \\ \mathcal{M}_h^k &= \{\boldsymbol{\mu} \in (L^2(\mathcal{E}_h))^m : \boldsymbol{\mu}|_F \in (\mathcal{P}^k(F))^m, \forall F \in \mathcal{E}_h\} \end{aligned}$$

for $\mathbf{a} = (a_i), 1 \leq i \leq m$, and $\mathbf{A} = (A_{ij}), 1 \leq i \leq m, 1 \leq j \leq d$. Here $L^2(D)$ is the space of square integrable functions on D . For functions \mathbf{a} and \mathbf{b} in $(L^2(D))^m$, we denote $(\mathbf{a}, \mathbf{b})_D = \int_D \mathbf{a} \cdot \mathbf{b}$ if D is a domain in \mathbb{R}^d

and $\langle \mathbf{a}, \mathbf{b} \rangle_D = \int_D \mathbf{a} \cdot \mathbf{b}$ if D is a domain in \mathbb{R}^{d-1} . For functions \mathbf{A} and \mathbf{B} in $(L^2(D))^{m \times d}$, we denote $(\mathbf{A}, \mathbf{B})_D = \int_D \text{tr}(\mathbf{A}^T \mathbf{B})$ if D is a domain in \mathbb{R}^d and $\langle \mathbf{A}, \mathbf{B} \rangle_D = \int_D \text{tr}(\mathbf{A}^T \mathbf{B})$ if D is a domain in \mathbb{R}^{d-1} , where tr is the trace operator of a square matrix. We introduce the following inner products

$$(\mathbf{a}, \mathbf{b})_{\mathcal{T}_h} = \sum_{K \in \mathcal{T}_h} (\mathbf{a}, \mathbf{b})_K, \quad (\mathbf{A}, \mathbf{B})_{\mathcal{T}_h} = \sum_{K \in \mathcal{T}_h} (\mathbf{A}, \mathbf{B})_K,$$

$$\langle \mathbf{a}, \mathbf{b} \rangle_{\partial \mathcal{T}_h} = \sum_{K \in \mathcal{T}_h} \langle \mathbf{a}, \mathbf{b} \rangle_{\partial K}, \quad \langle \mathbf{A}, \mathbf{B} \rangle_{\partial \mathcal{T}_h} = \sum_{K \in \mathcal{T}_h} \langle \mathbf{A}, \mathbf{B} \rangle_{\partial K}.$$

We are ready to define the HDG method for solving the system (19).

First, we rewrite the system (19) as a first-order system of equations as follows

$$\begin{aligned} \mathbf{Q} - \nabla \mathbf{u} &= 0, & \text{in } \Omega, \\ \nabla \cdot (\mathbf{F}(\mathbf{u}) - \lambda \mathbf{G}(\mathbf{u}, \mathbf{Q}, \eta)) &= 0, & \text{in } \Omega. \end{aligned} \quad (20)$$

The HDG method for the first-order system finds $(\mathbf{Q}_h, \mathbf{u}_h, \hat{\mathbf{u}}_h) \in \mathcal{Q}_h^k \times \mathcal{V}_h^k \times \mathcal{M}_h^k$ such that

$$(\mathbf{Q}_h, \mathbf{E})_{\mathcal{T}_h} + (\mathbf{u}_h, \nabla \cdot \mathbf{E})_{\mathcal{T}_h} - \langle \hat{\mathbf{u}}_h, \mathbf{E} \cdot \mathbf{n} \rangle_{\partial \mathcal{T}_h} = 0, \quad (21a)$$

$$- (\mathbf{F}(\mathbf{u}_h) - \lambda \mathbf{G}(\mathbf{u}_h, \mathbf{Q}_h, \eta), \nabla \mathbf{w})_{\mathcal{T}_h} + \langle \widehat{\mathbf{H}} \cdot \mathbf{n}, \mathbf{w} \rangle_{\partial \mathcal{T}_h} = 0, \quad (21b)$$

$$\langle \widehat{\mathbf{H}} \cdot \mathbf{n}, \boldsymbol{\mu} \rangle_{\partial \mathcal{T}_h \setminus \partial \Omega} + \langle \widehat{\mathbf{B}} \cdot \mathbf{n}, \boldsymbol{\mu} \rangle_{\partial \Omega} = 0, \quad (21c)$$

for all $(\mathbf{E}, \mathbf{w}, \boldsymbol{\mu}) \in \mathcal{Q}_h^k \times \mathcal{V}_h^k \times \mathcal{M}_h^k$, where

$$\widehat{\mathbf{H}} \cdot \mathbf{n} = (\mathbf{F}(\hat{\mathbf{u}}_h) - \lambda \mathbf{G}(\hat{\mathbf{u}}_h, \mathbf{Q}_h, \eta)) \cdot \mathbf{n} + \mathbf{A}(\mathbf{u}_h - \hat{\mathbf{u}}_h) \quad (22)$$

is the numerical flux and $\widehat{\mathbf{B}} \cdot \mathbf{n}$ is the boundary flux whose definition depends on the boundary conditions. Note that \mathbf{A} is the stabilization matrix which is in general a matrix-valued function of both \mathbf{u}_h and $\hat{\mathbf{u}}_h$. In this paper, we simply take $\mathbf{A} = \tau \mathbf{I}$ where τ is a constant function on the physical domain. This completes the definition of the HDG method for solving the system (19). We will not discuss the implementation of the HDG method and refer to [51, 53, 54, 41, 57] for the detailed discussion.

3.2. Continuous Galerkin method

We describe the CG method for solving the following Helmholtz problem

$$\eta - \kappa^2 \nabla^2 \eta = s(\mathbf{u}_h, \mathbf{Q}_h) \quad \text{in } \Omega, \quad (23)$$

subject to a homogeneous Neumann condition $\nabla \eta \cdot \mathbf{n} = 0$ on $\partial\Omega$, where \mathbf{u}_h and \mathbf{Q}_h are already computed by using the HDG method. Recall that $\kappa = h_{\min}$, where h_{\min} is the smallest edge over all elements in $\mathcal{T}_h^{\text{shock}}$. The CG method finds an approximate solution $\eta_h \in \mathcal{W}_h^k$ such that it satisfies

$$\int_{\Omega} \eta_h w d\mathbf{x} + \kappa^2 \int_{\Omega} \nabla \eta_h \cdot \nabla w d\mathbf{x} = \int_{\Omega} s(\mathbf{u}_h, \mathbf{Q}_h) w d\mathbf{x}, \quad \forall w \in \mathcal{W}_h^k. \quad (24)$$

Here the finite element space \mathcal{W}_h^k is given by

$$\mathcal{W}_h^k = \{w \in C^0(\mathcal{T}_h) : w|_K \in (\mathcal{P}^k(K)), \forall K \in \mathcal{T}_h\}. \quad (25)$$

The same polynomial degree k is used to approximate the artificial viscosity. Of course, the numerical solution of the Helmholtz equation is many times less expensive than that of the regularized conservation laws.

We note that the source term s in (23) is a function of both \mathbf{u}_h and \mathbf{Q}_h , which are discontinuous approximate variables of polynomial degree k . Hence, s is high-order and discontinuous across element boundaries, whereas η is continuous and high-order field. Other PDE-based artificial viscosity methods define the source term s as a piecewise-constant function in terms of an appropriate scalar variable such as pressure or density [27, 38].

4. Numerical Results

In this section, we present numerical results for a number of inviscid steady-state problems to demonstrate the adaptive viscosity regularization approach. The initial artificial viscosity is set to $\eta_0(\mathbf{x}) = \tanh(20d(\mathbf{x}))$, where $d(\mathbf{x})$ is a distance from $\mathbf{x} \in \Omega$ to the wall boundary Γ_{wall} . Hence, η_0 is equal to 1 on most of the physical domain and vanishes smoothly to zero at the wall boundary. This choice is made because adding viscosity on the entire wall boundary can affect the wall boundary conditions, which may negatively impact the accuracy and convergence of the numerical solution near the wall. The initial regularization parameter λ_0 is chosen large enough so that the initial numerical solution \mathbf{u}_0 is smooth, but not necessarily accurate. For

all the problems, the homotopy parameter η is set 0.8 and the source term threshold S_0 is set to 0.5. We use polynomial degree $k = 4$ to represent the approximate solutions. The approach is found to be so robust that there is no need to use time continuation or polynomial degree continuation to compute steady-state solutions.

4.1. Inviscid Burgers' equation

We consider the two-dimensional space-time inviscid Burgers' equation [46]:

$$\frac{\partial u}{\partial t} + \frac{1}{2} \frac{\partial u^2}{\partial x} = 0 \quad \text{in } \Omega \equiv (-1, 1) \times (0, 1), \quad (26)$$

with boundary condition $u(x, t) = 2(x+1)^2(1-H(x))$ on $\Gamma_D \equiv \{x = 0\} \cup \{t = 0\}$, where $H(x)$ is the step function. The exact solution is given by

$$u(x, t) = \begin{cases} U(x, t) & x < x_s(t) \\ 0 & x > x_s(t) \end{cases} \quad (27)$$

where $U(x, t)$ is found by solving the quadratic equation $U = 2(x - Ut + 1)^2$. The exact shock location $x_s(t)$ is the solution of the following ordinary differential equation

$$\frac{dx_s}{dt} = \frac{U(x_s, t)}{2}, \quad x_s(0) = 0. \quad (28)$$

We use an initial uniform mesh of 288 $k = 4$ elements to obtain an approximate solution which is shown in Figure 6(a). This solution is compared to the numerical approximation on a shock-aligned mesh of 523 $k = 4$ elements which is generated by means of the procedure described in Section 2.5.

The resulting shock location and shock-aligned mesh are shown in Figure 5. We observe that the shock location, which is identified based on the approximate solution on the uniform mesh, accurately approximates the exact shock location. Figure 6(b) shows the artificial viscosity and the approximate solution on the shock-aligned mesh.

We see that the artificial viscosity on the shock-aligned mesh is about 100 times smaller than that on the regular mesh. The approximate solution on the shock-aligned mesh is sharper and more accurate than that on the regular mesh. This can also be seen in Figure 7, which displays both the exact and approximate solutions. We see that the approximate solution on the shock-aligned mesh is almost indistinguishable from the exact solution.

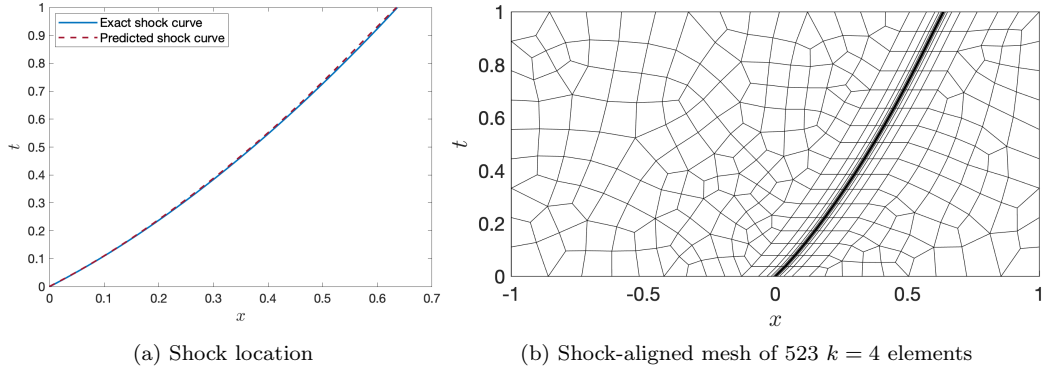


Figure 5: Shock location and shock-aligned mesh for the inviscid Burgers' equation.

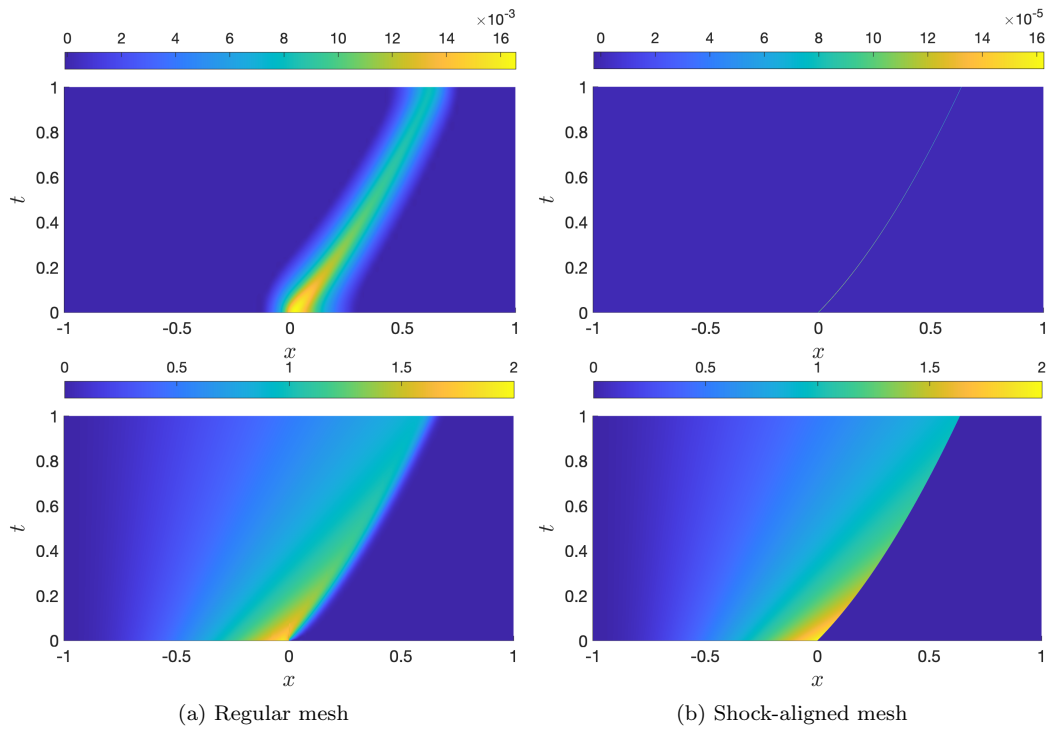


Figure 6: Artificial viscosity (top) and approximate solution (bottom) for the inviscid Burgers' equation.

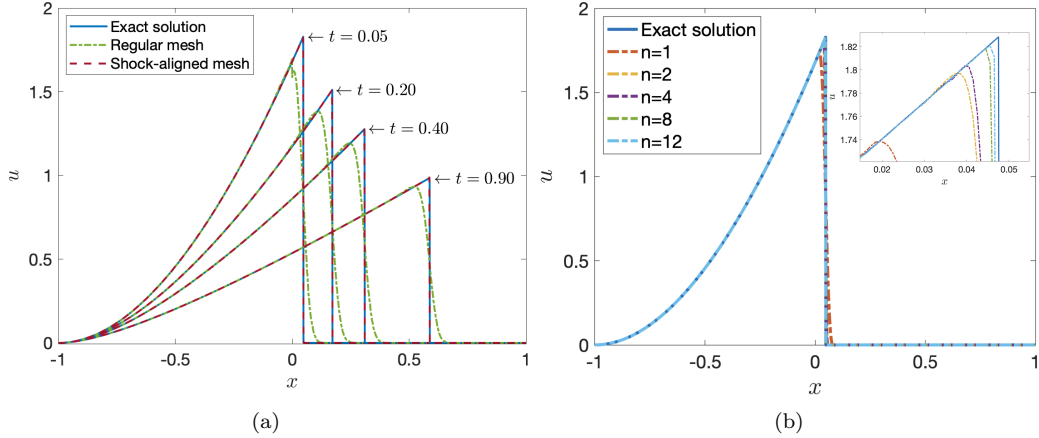


Figure 7: Comparison of the approximate solution and the exact solution for the inviscid Burgers' equation. (a) Profiles of the exact and approximate solutions at different times. (b) Profiles of the approximate solution for different homotopy iterations n at $t = 0.05$.

4.2. Inviscid transonic flow past NACA 0012 airfoil

The second example involves a case of transonic flow past a NACA 0012 airfoil at angle of attack $\alpha = 1.5^\circ$ and freestream Mach number $M_\infty = 0.8$ [16]. A shock is formed on the upper surface, while another weaker shock is formed under the lower surface. Figure 8 depicts the initial unstructured grid of 1082 elements and a shock-aligned mesh of 1769 elements. The close-up view of these two meshes near the NACA 0012 airfoil is shown in Figure 4.

Figure 9 shows the pressure computed on the regular mesh and the shock-aligned mesh. As expected, the shock-aligned mesh yields a sharper, smoother, and more accurate solution than the regular mesh. This can be clearly seen from the profiles of the computed pressure and Mach number in Figure 11. We see that the shocks are captured very well by using our method to compute the solution on the shock-aligned mesh. Away from the shock region, the computed solutions match with each other. Figure 10 depicts artificial viscosity and Mach number computed on the shock-aligned mesh at different homotopy iterations. We note that the amount of artificial viscosity is reduced as n increases, resulting in sharper shock profiles and more accurate solutions.

4.3. Inviscid supersonic flow past unit circular cylinder

The third test case is the supersonic flow past a unit circular cylinder at $M_\infty = 3$. A strong bow shock forms in front of the cylinder. Part of

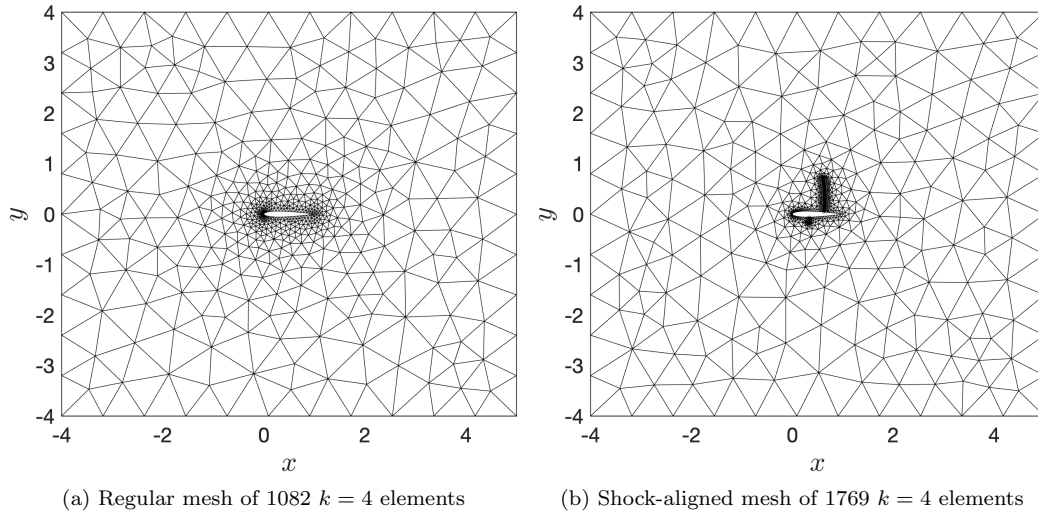


Figure 8: Computational meshes for inviscid flow past NACA 0012 airfoil at $M_\infty = 0.8$ and 1.5° angle of attack.

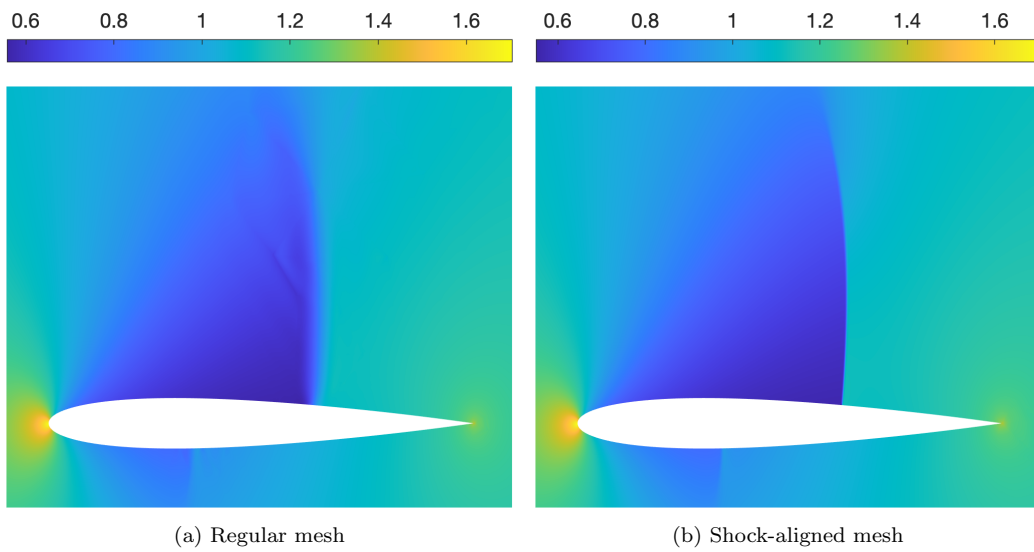


Figure 9: Computed pressure for inviscid flow past NACA 0012 airfoil at $M_\infty = 0.8$ and 1.5° angle of attack.

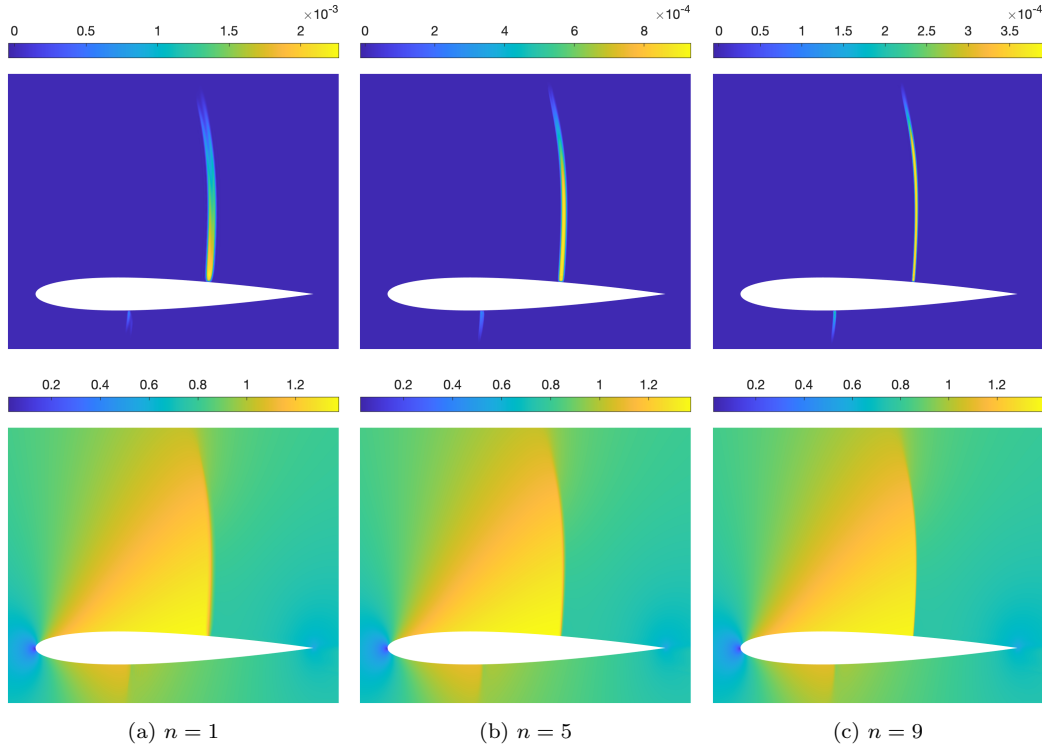


Figure 10: Artificial viscosity (top row) and Mach number (bottom row) at different homotopy iterations on the shock-aligned mesh for inviscid flow past NACA 0012 airfoil at $M_\infty = 0.8$ and 1.5° angle of attack.

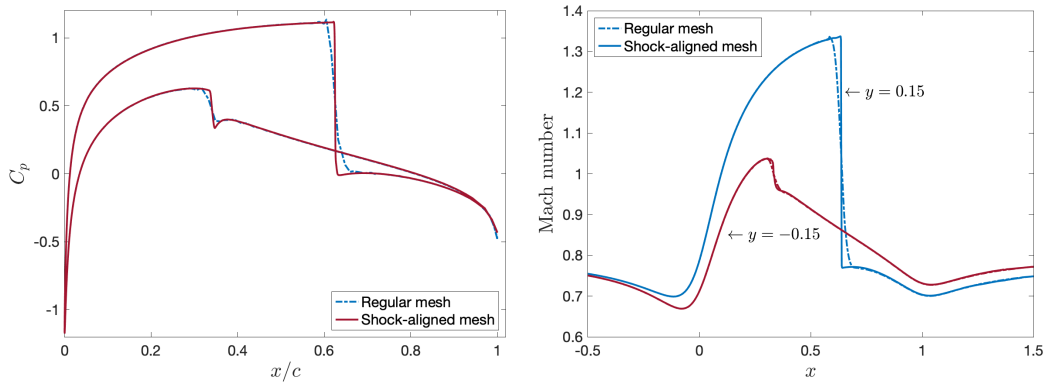


Figure 11: Profiles of computed pressure on the upper and lower surfaces of the airfoil (left) and Mach number along horizontal lines $y = \pm 0.15$ (right) for inviscid flow past NACA 0012 airfoil at $M_\infty = 0.8$ and 1.5° angle of attack.

the flow region behind the shock is subsonic. The cylinder wall is modeled with inviscid wall boundary condition. Supersonic outflow boundary conditions are used at the outflow boundaries, while the rest of the boundary features supersonic inflow conditions. This test case serves to demonstrate the effectiveness of our approach for supersonic shocks.

We show the regular mesh and the shock-align mesh in Figure 12, and profiles of density and Mach number along $y = 0$ in Figure 13 at different homotopy iterations. We see that the shock profiles get sharper as n increases. Furthermore, the shock profiles on the shock-aligned mesh are considerably sharper than those on the regular mesh. Figure 14 and Figure 15 depict the solutions computed on the regular mesh and the shock-aligned mesh, respectively. The magnitude and width of artificial viscosity are considerably reduced as n increases, indicating a significant reduction of the amount of artificial viscosity. Furthermore, the shock-aligned mesh yields much smaller and narrower artificial viscosity than the regular mesh. As a result, the solutions computed on the shock-aligned mesh are more accurate than those on the regular mesh, as it can be clearly seen from the computed enthalpy and Mach number.

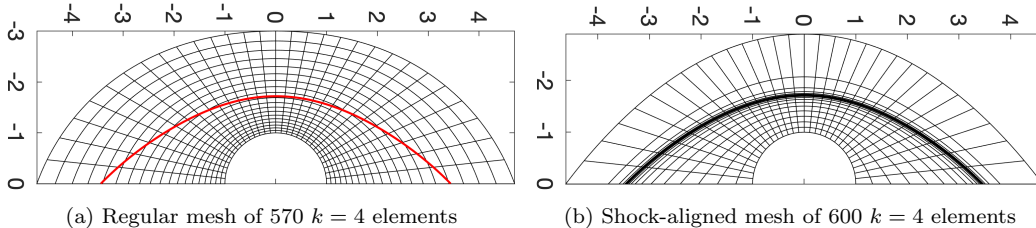


Figure 12: Computational meshes for inviscid flow past the circular cylinder at $M_\infty = 3$. The red curve indicates the location of the bow shock identified using the approximate solution on the regular mesh. The meshes are rotated 90 degrees to save spaces.

Table 1 tabulates relevant quantities of interest as a function of the homotopy iteration n on the shock-aligned mesh. In this, $\theta_n = \sigma(\lambda_n, \kappa_n)/\sigma(\lambda_1, \kappa_1)$, $\|\varepsilon_n\|_\Omega$ is the L_2 norm of the artificial viscosity field on the physical domain, $\|M_n\|_\infty$ is the L_∞ norm of the Mach number, $e_n^H = \|H_n - H_{\text{exact}}\|_{\Omega \setminus \Omega^{\text{shock}}}$ is the L_2 norm of the enthalpy error on the smooth domain, $\rho_n(\mathbf{x}^*)$ and $p_n(\mathbf{x}^*)$ are the values of density and pressure at the stagnation point $\mathbf{x}^* = (-1, 0)$. The homotopy continuation ends at $n = 10$ where $\theta_{10} = 5.4388$ is greater than the specified threshold. We see that the amount of artificial viscosity (namely, $\|\varepsilon_n\|_\Omega$) and the enthalpy error (namely, e_n^H) decrease as n increases.

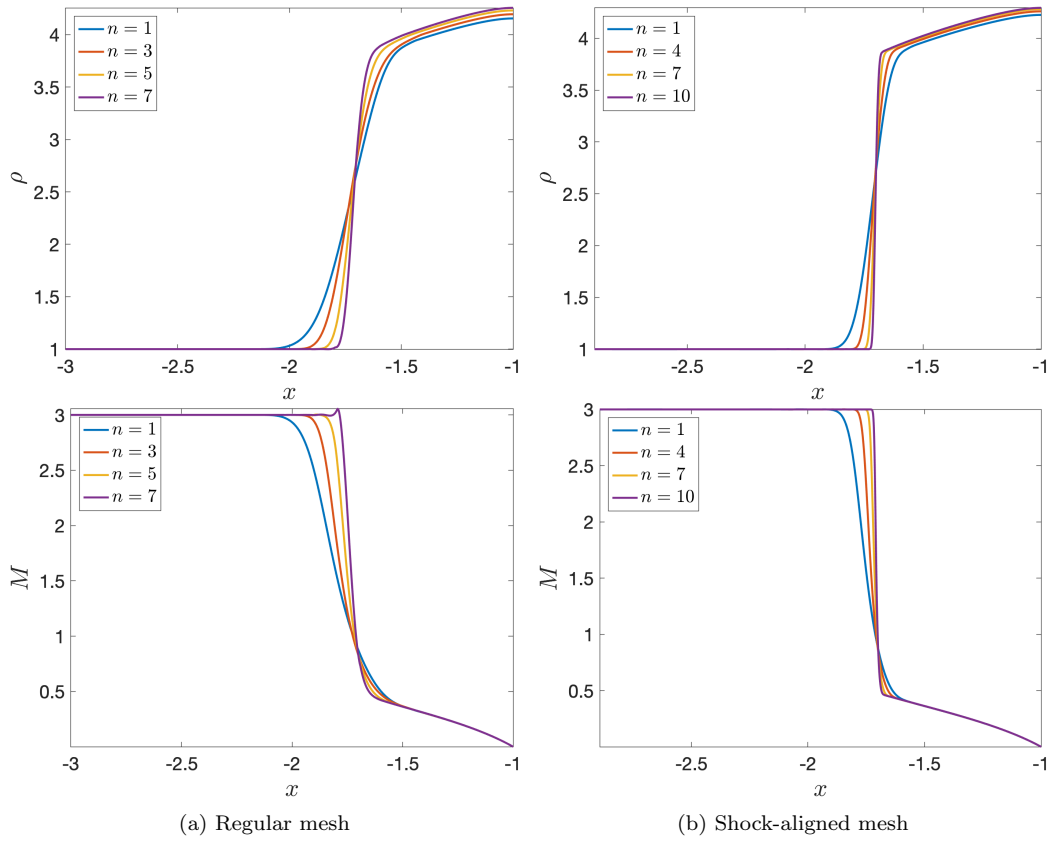


Figure 13: Profiles of density (top) and Mach number (bottom) along $y = 0$ at different homotopy iterations for inviscid flow past the cylinder at $M_\infty = 3$.

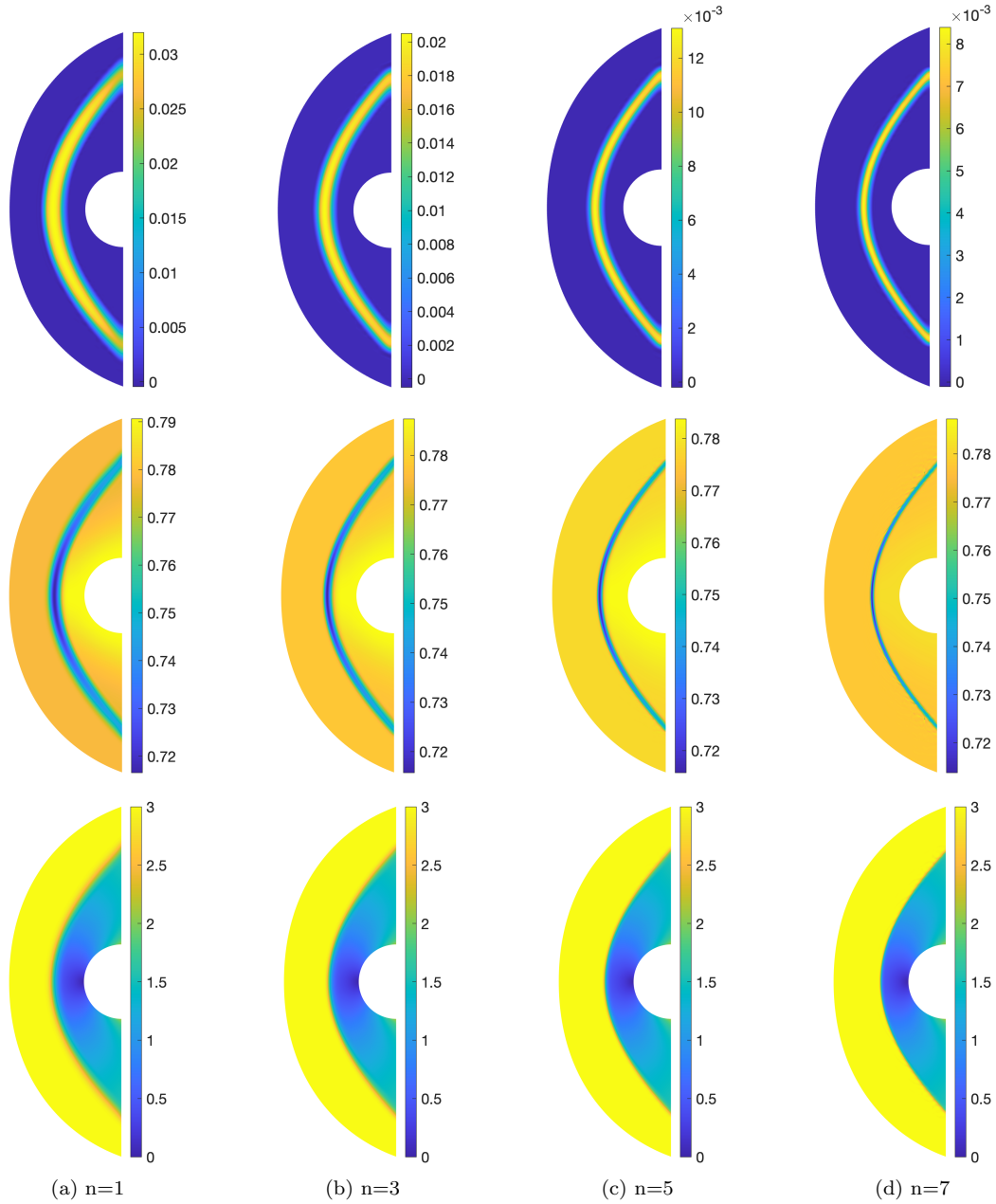


Figure 14: Computed artificial viscosity (top row), enthalpy (middle row), and Mach number (bottom row) at different homotopy iterations on the regular mesh for inviscid supersonic flow past the cylinder at $M_\infty = 3$.

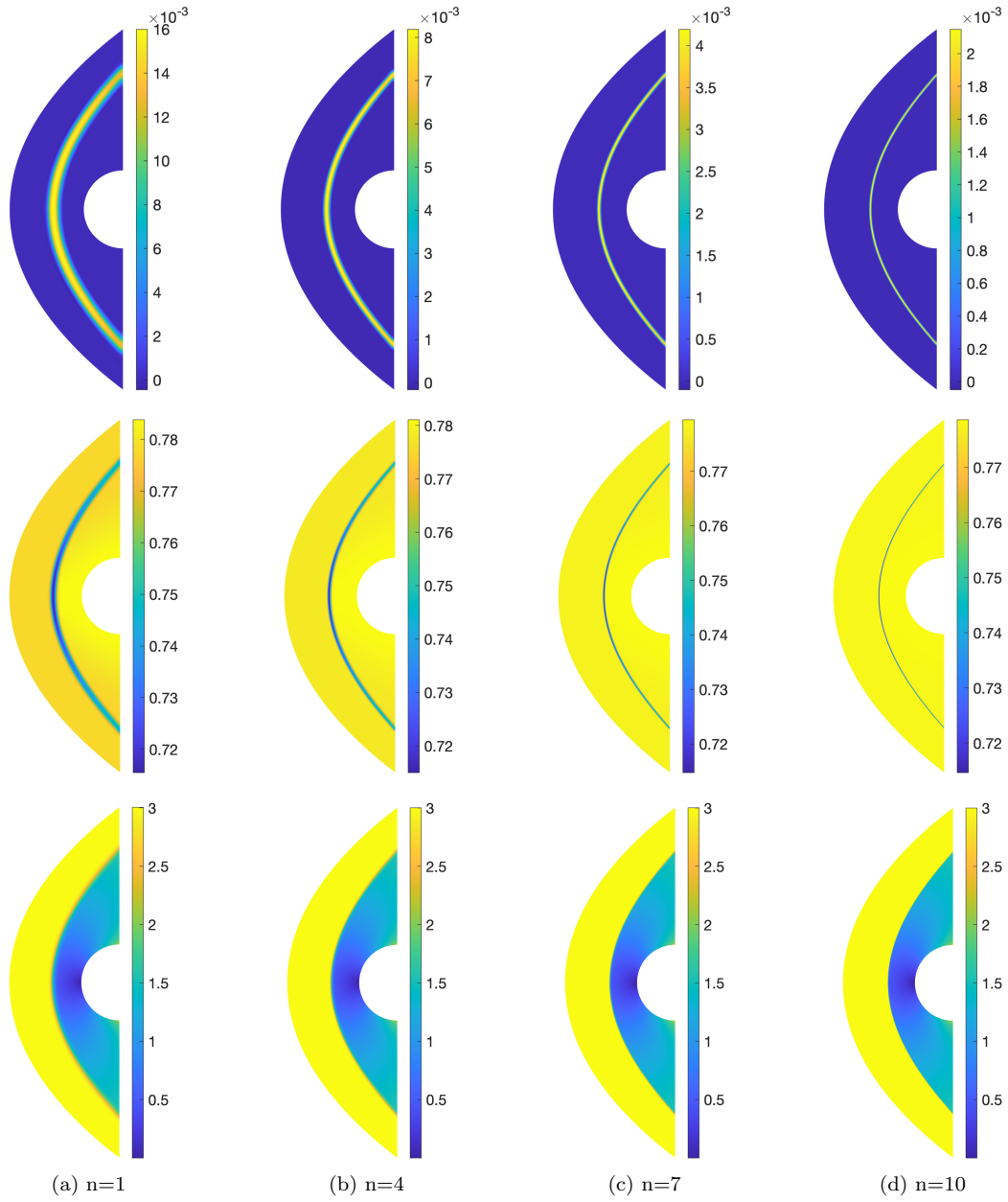


Figure 15: Computed artificial viscosity (top row), enthalpy (middle row), and Mach number (bottom row) at different homotopy iterations on the shock-aligned mesh for inviscid supersonic flow past the cylinder at $M_\infty = 3$.

The results clearly show that the amount of artificial viscosity affects the accuracy of the approximate solution not only in the shock region but also away from the shock region. In particular, both the density and pressure at the stagnation point increase as the amount of artificial viscosity decreases. Moreover, the bow shock is very well captured since the overshoot in the Mach number is quite small as $\|M_n\|_\infty$ is close to $M_\infty = 3$.

n	γ_n	κ_n	θ_n	$\ \varepsilon_n\ _\Omega$	e_n^H	$\ M_n\ _\infty$	$\rho_n(\mathbf{x}^*)$	$p_n(\mathbf{x}^*)$
1	0.0200	5.0000	1.0000	0.0186	0.0096	3.0057	4.2263	0.9465
2	0.0160	4.2000	1.9725	0.0137	0.0084	3.0169	4.2364	0.9478
3	0.0128	3.5600	1.8190	0.0099	0.0066	3.0017	4.2498	0.9495
4	0.0102	3.0480	2.6473	0.0072	0.0055	3.0002	4.2607	0.9509
5	0.0082	2.6384	2.8580	0.0052	0.0043	3.0025	4.2697	0.9520
6	0.0066	2.3107	3.2740	0.0038	0.0038	3.0043	4.2770	0.9530
7	0.0052	2.0486	3.5356	0.0027	0.0030	3.0026	4.2828	0.9538
8	0.0042	1.8389	3.7983	0.0020	0.0025	3.0019	4.2876	0.9544
9	0.0034	1.6711	4.1949	0.0015	0.0020	3.0014	4.2914	0.9550
10	0.0027	1.5369	5.4388	0.0011	0.0017	3.0007	4.2945	0.9554

Table 1: Relevant quantities of interest as a function of homotopy iteration n for the approximate solutions computed on the shock-aligned mesh for inviscid hypersonic flow past the cylinder at $M_\infty = 3$.

4.4. Inviscid hypersonic flow past unit circular cylinder

The last test case involving hypersonic flow past a unit circular cylinder at $M_\infty = 7$ demonstrates the effectiveness of our approach for very strong shocks in the hypersonic regime. The boundary conditions are the same as those in the previous test case. The regular and the shock-aligned meshes are shown in Figure 16. Profiles of density computed on the shock-aligned mesh are shown in Figure 17 for different homotopy iterations. We see that the density profiles converge and get sharper as n increases. Figure 18 depicts the solution computed on the shock-aligned mesh. The artificial viscosity is reduced significantly as n increases. Furthermore, the solution converged at $n = 12$ is smooth and sharp. Table 2 tabulates relevant quantities of interest as a function of the homotopy iteration n on the shock-aligned mesh. The homotopy continuation ends at $n = 13$ where θ_{13} exceeds the specified threshold. We see that the amount of artificial viscosity (namely, $\|\varepsilon_n\|_\Omega$) and the enthalpy error (namely, e_n^H) decrease as n increases. The results

clearly show that the amount of artificial viscosity affects the accuracy of the approximate solution not only in the shock region but also away from the shock region. In particular, both the density and pressure at the stagnation point increase as the amount of artificial viscosity decreases. Moreover, the bow shock is very well captured since the overshoot in the Mach number is quite small as $\|M_n\|_\infty$ is close to $M_\infty = 7$. These observations are similar to those on the supersonic test case at $M_\infty = 3$.

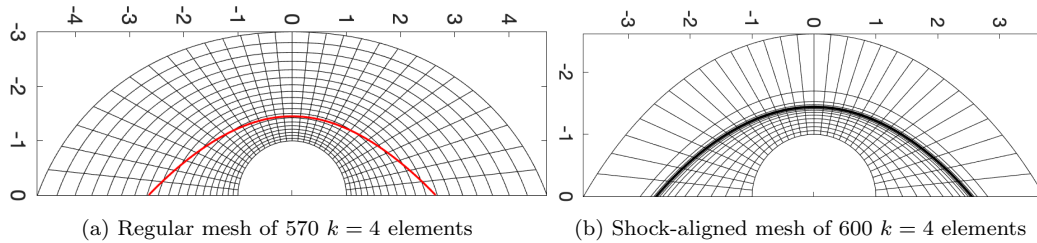


Figure 16: Meshes for inviscid hypersonic flow past the circular cylinder at $M_\infty = 7$.

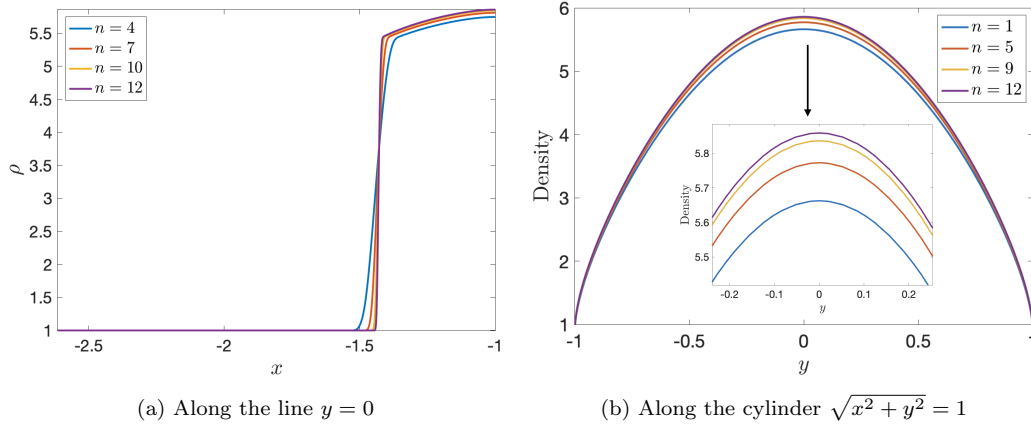


Figure 17: Profiles of density computed on the shock-aligned mesh for hypersonic flow past the cylinder at $M_\infty = 7$.

5. Concluding remarks

We have presented an adaptive artificial viscosity regularization approach for the numerical approximation of shock waves. The method couples a set of nonlinear conservation laws with an additional Helmholtz equation

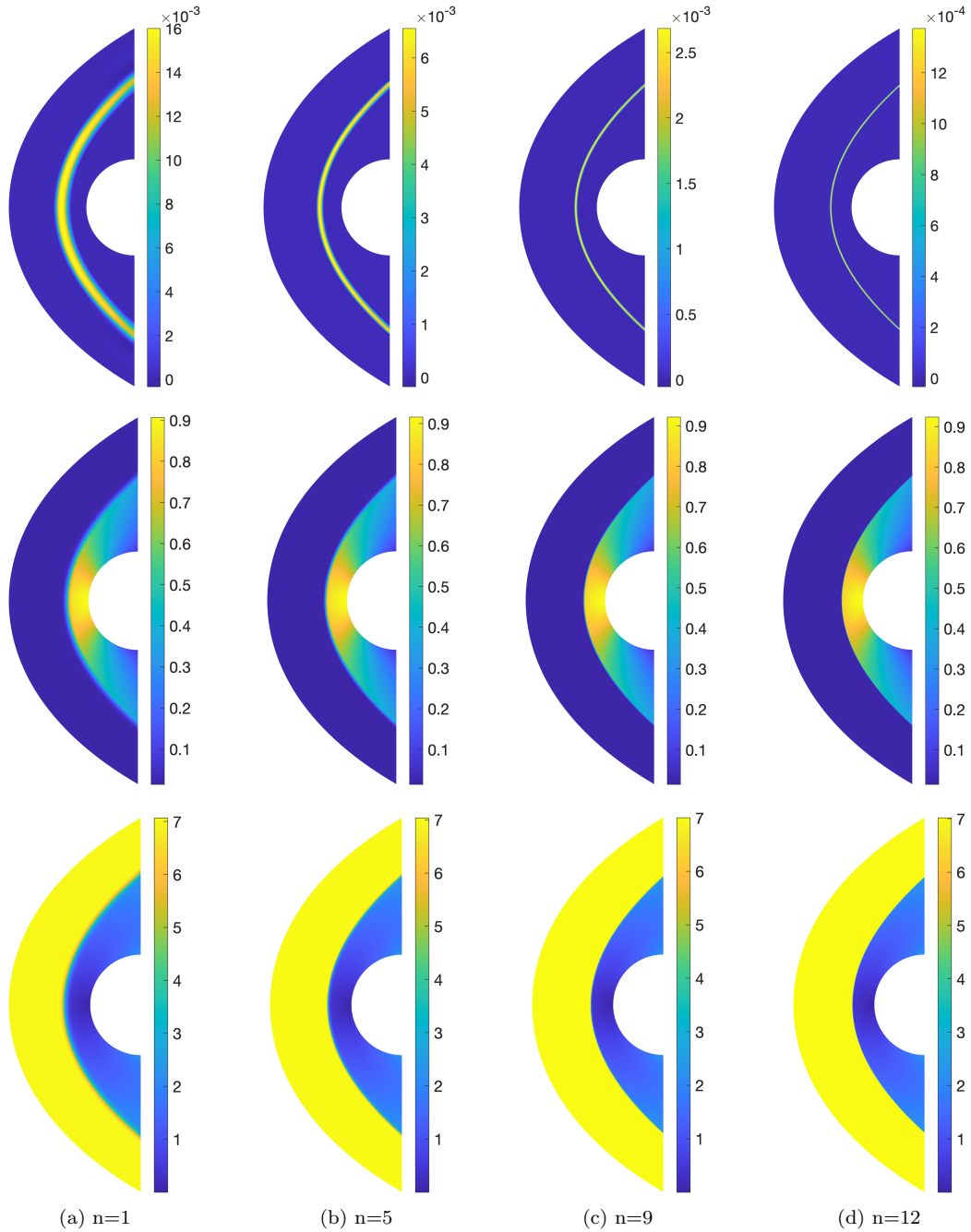


Figure 18: Computed artificial viscosity (top row), pressure (middle row), and Mach number (bottom row) at different homotopy iterations on the shock-aligned mesh for inviscid hypersonic flow past the cylinder at $M_\infty = 7$.

n	γ_n	κ_n	θ_n	$\ \varepsilon_n\ _\Omega$	e_n^H	$\ M_n\ _\infty$	$\rho_n(\mathbf{x}^*)$	$p_n(\mathbf{x}^*)$
1	0.0200	5.0000	1.0026	0.0153	0.0111	7.0533	5.6627	0.9069
2	0.0160	4.2000	1.0000	0.0109	0.0108	7.5869	5.6755	0.9083
3	0.0128	3.5600	1.1959	0.0080	0.0087	7.1191	5.7146	0.9114
4	0.0102	3.0480	1.4298	0.0059	0.0069	7.0422	5.7472	0.9141
5	0.0082	2.6384	1.6255	0.0042	0.0056	7.0113	5.7727	0.9162
6	0.0066	2.3107	1.8670	0.0030	0.0046	7.0233	5.7937	0.9181
7	0.0052	2.0486	2.0450	0.0022	0.0036	7.0038	5.8111	0.9196
8	0.0042	1.8389	2.1374	0.0016	0.0030	7.0056	5.8249	0.9209
9	0.0034	1.6711	2.2507	0.0011	0.0024	7.0023	5.8363	0.9219
10	0.0027	1.5369	2.1059	0.0008	0.0020	7.0005	5.8454	0.9227
11	0.0021	1.4295	2.8960	0.0006	0.0016	7.0006	5.8528	0.9234
12	0.0017	1.3436	4.1467	0.0004	0.0013	7.0133	5.8588	0.9240

Table 2: Relevant quantities of interest as a function of homotopy iteration n on the shock-aligned mesh for inviscid hypersonic flow past the cylinder at $M_\infty = 7$.

that defines a PDE-based artificial viscosity field. The procedure features an homotopy continuation of the regularization parameters that minimizes the amount of artificial viscosity needed to stabilize the shock waves, while enforcing positivity-preserving and smoothness constraints on the numerical solution. The approach is general for any kind of mesh but it is also combined with a mesh adaptation procedure that aligns the grid with shocks in order to further reduce the amount of viscosity and provide sharper and more accurate approximations.

The numerical methodology is solved using finite element methods. In particular, the HDG method used to discretize the set of governing equations is combined with the CG method, employed to solve the Helmholtz equation and provide an inherently continuous viscosity field. The approach is found to be robust and efficient enough so that no time or polynomial continuation processes are required for steady-state problems, converging to the optimal shock approximation in around 10 homotopy iterations.

We have presented a set of numerical examples featuring the inviscid Burgers' equation and inviscid transonic, supersonic and supersonic flows in two dimensions in order to demonstrate the performance of the method. The approach is able to produce a sequence of approximate solutions that converge to the exact solution, producing sharp representations of the shock waves, and smooth and non-oscillatory fields everywhere else.

The procedure here presented can be extended to the solution of com-

pressible viscous flows or chemically reacting flows without loss of generality. To this end, different variants of the regularized viscosity can be devised, including physics-based artificial viscosity terms that augment the molecular viscous components. On the other hand, the proposed methodology can be also coupled to shock-alignment of shock-fitting strategies, providing increased robustness in the iterative grid adaptation process. In this sense, an iterative procedure stemming from the proposed shock-aligned mesh generation algorithm could be automated.

Acknowledgements

We gratefully acknowledge the United States Department of Energy under contract DE-NA0003965, the National Science Foundation for supporting this work (under grant number NSF-PHY-2028125), and the Air Force Office of Scientific Research under Grant No. FA9550-22-1-0356 for supporting this work.

References

- [1] A. W. Cook, W. H. Cabot, A high-wavenumber viscosity for high-resolution numerical methods, *Journal of Computational Physics* 195 (2) (2004) 594–601. doi:10.1016/j.jcp.2003.10.012.
URL <http://linkinghub.elsevier.com/retrieve/pii/S0021999103005746>
- [2] A. W. Cook, W. H. Cabot, Hyperviscosity for shock-turbulence interactions, *Journal of Computational Physics* 203 (2) (2005) 379–385. doi:10.1016/j.jcp.2004.09.011.
URL <http://linkinghub.elsevier.com/retrieve/pii/S0021999104004000>
- [3] B. Fiorina, S. K. Lele, An artificial nonlinear diffusivity method for supersonic reacting flows with shocks, *Journal of Computational Physics* 222 (1) (2007) 246–264. doi:10.1016/j.jcp.2006.07.020.
- [4] S. Kawai, S. Lele, Localized artificial diffusivity scheme for discontinuity capturing on curvilinear meshes, *Journal of Computational Physics* 227 (22) (2008) 9498–9526. doi:10.1016/j.jcp.2008.06.034.
URL <http://linkinghub.elsevier.com/retrieve/pii/S0021999108003641>

- [5] S. Kawai, S. K. Shankar, S. K. Lele, Assessment of localized artificial diffusivity scheme for large-eddy simulation of compressible turbulent flows, *Journal of Computational Physics* 229 (5) (2010) 1739–1762. doi:10.1016/j.jcp.2009.11.005.
URL <http://linkinghub.elsevier.com/retrieve/pii/S0021999109006160>
- [6] A. Klöckner, T. Warburton, J. S. Hesthaven, Viscous shock capturing in a time-explicit discontinuous Galerkin method, *Mathematical Modelling of Natural Phenomena* 6 (3) (2011) 57–83. arXiv:1102.3190, doi:10.1051/mmnp/20116303.
- [7] L. Krivodonova, J. Xin, J.-F. Remacle, N. Chevaugeon, J. E. Flaherty, Shock detection and limiting with discontinuous Galerkin methods for hyperbolic conservation laws, *Appl. Numer. Math.* 48 (3-4) (2004) 323–338. doi:10.1016/j.apnum.2003.11.002.
URL <http://dx.doi.org/10.1016/j.apnum.2003.11.002>
- [8] A. Mani, J. Larsson, P. Moin, Suitability of artificial bulk viscosity for large-eddy simulation of turbulent flows with shocks, *Journal of Computational Physics* 228 (19) (2009) 7368–7374. doi:10.1016/j.jcp.2009.06.040.
URL <http://linkinghub.elsevier.com/retrieve/pii/S0021999109003623>
- [9] B. J. Olson, S. K. Lele, Directional artificial fluid properties for compressible large-eddy simulation, *Journal of Computational Physics* 246 (2013) 207–220. doi:10.1016/j.jcp.2013.03.026.
- [10] P. O. Persson, J. Peraire, Sub-cell shock capturing for discontinuous Galerkin methods, in: *Collection of Technical Papers - 44th AIAA Aerospace Sciences Meeting, Vol. 2, Reno, Nevada, 2006*, pp. 1408–1420. doi:10.2514/6.2006-112.
- [11] P. O. Persson, Shock capturing for high-order discontinuous Galerkin simulation of transient flow problems, in: *21st AIAA Computational Fluid Dynamics Conference, San Diego, CA, 2013*, p. 3061. doi:10.2514/6.2013-3061.

- [12] S. Premasuthan, C. Liang, A. Jameson, Computation of Flows With Shocks using the Spectral Difference method with Artificial Viscosity: Part I, *Computers & Fluids* 98 (2013) 111–121.
- [13] S. Premasuthan, C. Liang, A. Jameson, Computation of flows with shocks using the Spectral Difference method with artificial viscosity, II: Modified formulation with local mesh refinement, *Computers & Fluids* 98 (2014) 122–133.
- [14] P. Fernandez, N. C. Nguyen, J. Peraire, A physics-based shock capturing method for unsteady laminar and turbulent flows, in: 56th AIAA Aerospace Sciences Meeting, Orlando, Florida, 2018, pp. AIAA–2018–0062.
- [15] D. Moro, N. C. Nguyen, J. Peraire, Dilation-based shock capturing for high-order methods, *International Journal for Numerical Methods in Fluids* 82 (7) (2016) 398–416. doi:10.1002/flid.4223.
- [16] N. C. Nguyen, J. Perairey, An adaptive shock-capturing HDG method for compressible flows, in: 20th AIAA Computational Fluid Dynamics Conference 2011, American Institute of Aeronautics and Astronautics, Reston, Virginia, 2011, pp. AIAA 2011–3060. doi:10.2514/6.2011-3060.
URL <http://arc.aiaa.org/doi/abs/10.2514/6.2011-3060>
- [17] A. Burbeau, P. Sagaut, C. H. Bruneau, A Problem-Independent Limiter for High-Order Runge-Kutta Discontinuous Galerkin Methods, *Journal of Computational Physics* 169 (1) (2001) 111–150. doi:10.1006/jcph.2001.6718.
- [18] B. Cockburn, C.-W. Shu, TVB Runge-Kutta Local Projection Discontinuous Galerkin Finite Element Method for Conservation Laws II: General Framework, *Mathematics of Computation* 52 (186) (1989) 411. doi:10.2307/2008474.
- [19] L. Krivodonova, Limiters for high-order discontinuous Galerkin methods, *Journal of Computational Physics* 226 (1) (2007) 879–896.
- [20] B. Cockburn, C. W. Shu, The Runge-Kutta Discontinuous Galerkin Method for Conservation Laws V: Multidimensional Systems, *Journal*

- of Computational Physics 141 (2) (1998) 199–224. doi:10.1006/jcph.1998.5892.
- [21] Y. Lv, M. Ihme, Entropy-bounded discontinuous Galerkin scheme for Euler equations, *Journal of Computational Physics* 295 (2015) 715–739. arXiv:1411.5044, doi:10.1016/j.jcp.2015.04.026.
- [22] M. Sonntag, C. D. Munz, Efficient Parallelization of a Shock Capturing for Discontinuous Galerkin Methods using Finite Volume Subcells, *Journal of Scientific Computing* 70 (3) (2017) 1262–1289. doi:10.1007/s10915-016-0287-5.
- [23] H. Luo, J. D. Baum, R. Löhner, A Hermite WENO-based limiter for discontinuous Galerkin method on unstructured grids, *Journal of Computational Physics* 225 (1) (2007) 686–713. doi:10.1016/j.jcp.2006.12.017.
- [24] J. Qiu, C. W. Shu, Runge-Kutta discontinuous Galerkin method using WENO limiters, *SIAM Journal on Scientific Computing* 26 (3) (2005) 907–929. doi:10.1137/S1064827503425298.
- [25] J. Zhu, J. Qiu, C. W. Shu, M. Dumbser, Runge-Kutta discontinuous Galerkin method using WENO limiters II: Unstructured meshes, *Journal of Computational Physics* 227 (9) (2008) 4330–4353. doi:10.1016/j.jcp.2007.12.024.
- [26] J. Zhu, X. Zhong, C. W. Shu, J. Qiu, Runge-Kutta discontinuous Galerkin method using a new type of WENO limiters on unstructured meshes, *Journal of Computational Physics* 248 (2013) 200–220. doi:10.1016/j.jcp.2013.04.012.
- [27] G. E. Barter, D. L. Darmofal, Shock capturing with PDE-based artificial viscosity for DGFEM: Part I. Formulation, *Journal of Computational Physics* 229 (5) (2010) 1810–1827. doi:10.1016/j.jcp.2009.11.010.
URL <http://linkinghub.elsevier.com/retrieve/pii/S0021999109006299>
- [28] R. Hartmann, Higher-order and adaptive discontinuous Galerkin methods with shock-capturing applied to transonic turbulent delta wing flow, *International Journal for Numerical Methods in Fluids* 72 (2013) 883–894.

- [29] Y. Lv, Y. C. See, M. Ihme, An entropy-residual shock detector for solving conservation laws using high-order discontinuous Galerkin methods, *Journal of Computational Physics* 322 (2016) 448–472. doi: 10.1016/j.jcp.2016.06.052.
- [30] H. Abbassi, F. Mashayek, G. B. Jacobs, Shock capturing with entropy-based artificial viscosity for staggered grid discontinuous spectral element method, *Computers & Fluids* 98 (2014) 152–163.
- [31] A. Chaudhuri, G. B. Jacobs, W. S. Don, H. Abbassi, F. Mashayek, Explicit discontinuous spectral element method with entropy generation based artificial viscosity for shocked viscous flows, *Journal of Computational Physics* 332 (2017) 99–117. doi:10.1016/j.jcp.2016.11.042.
- [32] E. Johnsen, J. Larsson, A. V. Bhagatwala, W. H. Cabot, P. Moin, B. J. Olson, P. S. Rawat, S. K. Shankar, B. Sjögren, H. Yee, X. Zhong, S. K. Lele, Assessment of high-resolution methods for numerical simulations of compressible turbulence with shock waves, *Journal of Computational Physics* 229 (4) (2010) 1213–1237. doi:10.1016/j.jcp.2009.10.028. URL <http://linkinghub.elsevier.com/retrieve/pii/S0021999109005804>
- [33] J. Von Neumann, R. D. Richtmyer, A method for the numerical calculation of hydrodynamic shocks, *Journal of Applied Physics* 21 (1950) 232–237.
- [34] A. Jameson, Analysis and Design of Numerical Schemes for Gas Dynamics, 2: Artificial Diffusion and Discrete Shock Structure, *International Journal of Computational Fluid Dynamics* 5 (1995) 1–38.
- [35] T. J. Hughes, M. Mallet, M. Akira, A new finite element formulation for computational fluid dynamics: II. Beyond SUPG, *Computer Methods in Applied Mechanics and Engineering* 54 (3) (1986) 341–355. doi: 10.1016/0045-7825(86)90110-6.
- [36] Y. Maday, S. O. Kaber, E. Tadmor, Legendre pseudospectral viscosity method for nonlinear conservation laws, *SIAM J. Numer. Anal.* 30 (1993) 321–342.
- [37] E. Tadmor, Convergence of spectral methods for nonlinear conservation laws, *SIAM J. Numer. Anal.* 26 (1989) 30–44.

- [38] E. J. Ching, Y. Lv, P. Gnoffo, M. Barnhardt, M. Ihme, Shock capturing for discontinuous Galerkin methods with application to predicting heat transfer in hypersonic flows, *Journal of Computational Physics* 376 (2019) 54–75. doi:10.1016/j.jcp.2018.09.016.
- [39] R. Hartmann, P. Houston, Adaptive discontinuous Galerkin finite element methods for the compressible Euler equations, *Journal of Computational Physics* 183 (2) (2002) 508–532. doi:10.1006/jcph.2002.7206.
- [40] Y. Bai, K. J. Fidkowski, Continuous Artificial-Viscosity Shock Capturing for Hybrid Discontinuous Galerkin on Adapted Meshes, *AIAA Journal* 60 (10) (2022) 5678–5691. doi:10.2514/1.J061783.
URL <https://doi.org/10.2514/1.J061783>
- [41] J. Vila-Pérez, M. Giacomini, R. Sevilla, A. Huerta, Hybridisable Discontinuous Galerkin Formulation of Compressible Flows, *Archives of Computational Methods in Engineering* 28 (2) (2021) 753–784. doi:10.1007/s11831-020-09508-z.
URL <https://doi.org/10.1007/s11831-020-09508-z>
- [42] A. Bhagatwala, S. K. Lele, A modified artificial viscosity approach for compressible turbulence simulations, *Journal of Computational Physics* 228 (14) (2009) 4965–4969. doi:10.1016/j.jcp.2009.04.009.
URL <http://linkinghub.elsevier.com/retrieve/pii/S0021999109002034>
- [43] A. W. Cook, Artificial fluid properties for large-eddy simulation of compressible turbulent mixing, *Physics of Fluids* 19 (5) (2007) 055103. doi:10.1063/1.2728937.
URL <http://link.aip.org/link/PHFLE6/v19/i5/p055103/s1{&}Agg=doi>
- [44] S. Premasuthan, C. Liang, A. Jameson, Computation Of Flows with Shocks Using Spectral Difference Scheme with Artificial Viscosity, in: 48th AIAA Aerospace Sciences Meeting, Orlando, FL, 2010.
- [45] M. J. Zahr, P. O. Persson, An optimization-based approach for high-order accurate discretization of conservation laws with discontinuous

- solutions, *Journal of Computational Physics* 365 (2018) 105–134. [arXiv:1712.03445](#), [doi:10.1016/j.jcp.2018.03.029](#).
- [46] M. J. Zahr, A. Shi, P. O. Persson, Implicit shock tracking using an optimization-based high-order discontinuous Galerkin method, *Journal of Computational Physics* 410 (2020) 109385. [arXiv:1912.11207](#), [doi:10.1016/j.jcp.2020.109385](#).
- [47] A. Shi, P. O. Persson, M. J. Zahr, Implicit shock tracking for unsteady flows by the method of lines, *Journal of Computational Physics* 454 (2022). [doi:10.1016/j.jcp.2021.110906](#).
- [48] A. Corrigan, A. D. Kercher, D. A. Kessler, A moving discontinuous Galerkin finite element method for flows with interfaces, *International Journal for Numerical Methods in Fluids* 89 (9) (2019) 362–406. [doi:10.1002/flid.4697](#).
- [49] A. D. Kercher, A. Corrigan, D. A. Kessler, The moving discontinuous Galerkin finite element method with interface condition enforcement for compressible viscous flows, *International Journal for Numerical Methods in Fluids* 93 (5) (2021) 1490–1519. [arXiv:2002.12740](#), [doi:10.1002/flid.4939](#).
- [50] A. D. Kercher, A. Corrigan, A least-squares formulation of the Moving Discontinuous Galerkin Finite Element Method with Interface Condition Enforcement, *Computers and Mathematics with Applications* 95 (2021) 143–171. [arXiv:2003.01044](#), [doi:10.1016/j.camwa.2020.09.012](#).
- [51] N. C. Nguyen, J. Peraire, Hybridizable discontinuous Galerkin methods for partial differential equations in continuum mechanics, *Journal of Computational Physics* 231 (18) (2012) 5955–5988. [doi:10.1016/j.jcp.2012.02.033](#).
 URL <http://linkinghub.elsevier.com/retrieve/pii/S0021999112001544>
- [52] P. Fernandez, A. Christophe, S. Terrana, N. C. Nguyen, J. Peraire, Hybridized discontinuous Galerkin methods for wave propagation, *Journal of Scientific Computing* 77 (3) (2018) 1566–1604. [doi:10.1007/s10915-018-0811-x](#).
 URL <http://link.springer.com/10.1007/s10915-018-0811-x>

- [53] D. Moro, N. C. Nguyen, J. Peraire, Navier-stokes solution using Hybridizable discontinuous Galerkin methods, in: 20th AIAA Computational Fluid Dynamics Conference 2011, American Institute of Aeronautics and Astronautics, Honolulu, Hawaii, 2011, pp. AIAA-2011-3407. doi:10.2514/6.2011-3407.
URL <http://arc.aiaa.org/doi/abs/10.2514/6.2011-3407>
- [54] J. Peraire, N. C. Nguyen, B. Cockburn, A hybridizable discontinuous Galerkin method for the compressible euler and Navier-Stokes equations, in: 48th AIAA Aerospace Sciences Meeting Including the New Horizons Forum and Aerospace Exposition, 2010, pp. AIAA 2010-363.
- [55] M. Woopen, A. Balan, G. May, J. Schütz, A comparison of hybridized and standard DG methods for target-based hp-adaptive simulation of compressible flow, *Computers and Fluids* 98 (2014) 3–16. doi:10.1016/j.compfluid.2014.03.023.
- [56] K. J. Fidkowski, A hybridized discontinuous Galerkin method on mapped deforming domains, *Computers and Fluids* 139 (2016) 80–91. doi:10.1016/j.compfluid.2016.04.004.
- [57] P. Fernandez, N. C. Nguyen, J. Peraire, The hybridized Discontinuous Galerkin method for Implicit Large-Eddy Simulation of transitional turbulent flows, *Journal of Computational Physics* 336 (2017) 308–329. doi:10.1016/j.jcp.2017.02.015.
- [58] D. Williams, An entropy stable, hybridizable discontinuous Galerkin method for the compressible Navier-Stokes equations, *Mathematics of Computation* 87 (309) (2018) 95–121.
- [59] S. Bianchini, A. Bressan, Vanishing viscosity solutions of nonlinear hyperbolic systems, *Annals of Mathematics* 161 (1) (2005) 223–342. arXiv:0111321, doi:10.4007/annals.2005.161.223.
- [60] N. Cuong Nguyen, S. Terrana, J. Peraire, Large-Eddy Simulation of Transonic Buffet Using Matrix-Free Discontinuous Galerkin Method, *AIAA Journal* 60 (5) (2022) 3060–3077. doi:10.2514/1.j060459.
- [61] C. Nguyen, S. Terrana, J. Peraire, Implicit Large eddy simulation of hypersonic boundary-layer transition for a flared cone, in: AIAA

SCITECH 2023 Forum, AIAA SciTech Forum, American Institute of Aeronautics and Astronautics, 2023, pp. AIAA 2023-0659. doi:10.2514/6.2023-0659.
URL <https://doi.org/10.2514/6.2023-0659>

- [62] C. Geuzaine, J. F. Remacle, Gmsh: A 3-D finite element mesh generator with built-in pre- and post-processing facilities, *International Journal for Numerical Methods in Engineering* 79 (11) (2009) 1309-1331. doi:10.1002/nme.2579.